

THE COBE DIFFUSE INFRARED BACKGROUND EXPERIMENT
 SEARCH FOR THE COSMIC INFRARED BACKGROUND:
 I. LIMITS AND DETECTIONS

M.G. Hauser¹, R.G. Arendt², T. Kelsall³, E. Dwek³, N. Odegard², J.L. Weiland², H.T. Freudenreich²,
 W.T. Reach⁴, R.F. Silverberg³, S.H. Moseley³, Y.C. Pei¹, P. Lubin⁵, J.C. Mather³, R.A. Shafer³,
 G.F. Smoot⁶, R. Weiss⁷, D.T. Wilkinson⁸, and E.L. Wright⁹

Received 1998 January 6; accepted 1998 June 3

ABSTRACT

The Diffuse Infrared Background Experiment (DIRBE) on the Cosmic Background Explorer (*COBE*) spacecraft was designed primarily to conduct a systematic search for an isotropic cosmic infrared background (CIB) in ten photometric bands from 1.25 to 240 μm . The results of that search are presented here. Conservative limits on the CIB are obtained from the minimum observed brightness in all-sky maps at each wavelength, with the faintest limits in the DIRBE spectral range being at 3.5 μm ($\nu I_\nu < 64 \text{ nW m}^{-2} \text{ sr}^{-1}$, 95% CL) and at 240 μm ($\nu I_\nu < 28 \text{ nW m}^{-2} \text{ sr}^{-1}$, 95% CL). The bright foregrounds from interplanetary dust scattering and emission, stars, and interstellar dust emission are the principal impediments to the DIRBE measurements of the CIB. These foregrounds have been modeled and removed from the sky maps. Assessment of the random and systematic uncertainties in the residuals and tests for isotropy show that only the 140 and 240 μm data provide candidate detections of the CIB. The residuals and their uncertainties provide CIB upper limits more restrictive than the dark sky limits at wavelengths from 1.25 to 100 μm . No plausible solar system or Galactic source of the observed 140 and 240 μm residuals can be identified, leading to the conclusion that the CIB has been detected at levels of $\nu I_\nu = 25 \pm 7$ and $14 \pm 3 \text{ nW m}^{-2} \text{ sr}^{-1}$ at 140 and 240 μm respectively. The integrated energy from 140 to 240 μm , $10.3 \text{ nW m}^{-2} \text{ sr}^{-1}$, is about twice the integrated optical light from the galaxies in the Hubble Deep Field, suggesting that star formation might have been heavily enshrouded by dust at high redshift. The detections and upper limits reported here provide new constraints on models of the history of energy-releasing processes and dust production since the decoupling of the cosmic microwave background from matter.

Subject headings: cosmology: observations — diffuse radiation — infrared: general

1. INTRODUCTION

The search for the cosmic infrared background (CIB) radiation is a relatively new field of observational cosmology. The term “CIB” itself has been used with various meanings in the literature; we define it here to mean all diffuse infrared radiation arising external to the Milky Way Galaxy. Measurement of this distinct radiative background, expected to arise from the cumulative

emissions of pregalactic, protogalactic, and evolved galactic systems, would provide new insight into the cosmic “dark ages” following the decoupling of matter from the cosmic microwave background (CMB) radiation (Partridge & Peebles 1967; Harwit 1970; Bond, Carr, & Hogan 1986, 1991; Franceschini et al. 1991, 1994; Fall, Charlot, & Pei 1996).

The search for the CIB is impeded by two fundamental challenges: there is no unique spectral signature of

¹ Space Telescope Science Institute, 3700 San Martin Drive, Baltimore, MD 21218

² Raytheon STX, Code 685, NASA Goddard Space Flight Center, Greenbelt, MD 20771

³ Code 685, NASA Goddard Space Flight Center, Greenbelt, MD 20771

⁴ California Institute of Technology, IPAC/JPL, MS 100-22, Pasadena, CA 91125

⁵ UCSB, Physics Department, Santa Barbara, CA 93106

⁶ Lawrence Berkeley Laboratory, Space Sciences Laboratory, Department of Physics, UC Berkeley, CA 94720

⁷ Massachusetts Institute of Technology, Room 20F-001, Department of Physics, Cambridge, MA 02139

⁸ Princeton University, Department of Physics, Jadwin Hall, Box 708, Princeton, NJ 08544

⁹ UCLA, Astronomy Department, Los Angeles, CA 90024

such a background, and there are many local contributors to the infrared sky brightness at all wavelengths, several of them quite bright. The lack of a distinct spectral signature arises in part because so many different sources of primordial luminosity are possible (e.g., Bond, Carr, & Hogan 1986), in part because the radiant characteristics of evolving galaxies are imperfectly known, and in part because the primary emissions at any epoch are then shifted into the infrared by the cosmic red-shift and possibly by dust absorption and re-emission. Hence, the present spectrum depends in a complex way on the characteristics of the luminosity sources, on their cosmic history, and on the dust formation history of the Universe.

Setting aside the difficult possibility of recognizing the CIB by its angular fluctuation spectrum (Bond, Carr, & Hogan 1991; Kashlinsky et al. 1996a, b), the only identifying CIB characteristic for which one can search is an isotropic signal. Possible evidence for an isotropic infrared background, or at least limits on emission in excess of local foregrounds, has been reported on the basis of very limited data from rocket experiments (Matsumoto et al. 1988; Matsumoto 1990; Noda et al. 1992; Kawada et al. 1994). Puget et al. (1996) have used data from the *COBE* Far Infrared Absolute Spectrophotometer (FIRAS) to conclude that there is tentative evidence for a CIB at submillimeter wavelengths. Indirect upper limits, and even possible lower limits, on the extragalactic infrared background have been inferred from the apparent attenuation of TeV γ -rays in propagation from distant sources (de Jager, Stecker, & Salamon 1994; Dwek & Slavin 1994; Biller et al. 1995; Stecker 1996; Stecker & de Jager 1997). However, the detection of TeV γ -rays from Markarian 421 recently reported by Krennrich et al. (1997) casts some doubt on the infrared background inferred in this manner. The integrated energy density of the CIB in units of the critical density might, on the basis of pre-*COBE* observations (Ressell & Turner 1990), exceed that of the CMB, $\Omega_{\text{CMB}} = 1 \times 10^{-4} h_{50}^{-2}$, and preliminary DIRBE results (Hauser 1995, 1996a, b) only set limits on the integrated CIB which are comparable to the energy density in the CMB.

Direct detection of the CIB requires a number of steps. One must solve the formidable observational problem of making absolute brightness measurements in the infrared. One must then discriminate and remove the strong signals from foregrounds arising from one's instrument or observing environment, the terrestrial atmosphere, the solar system, and the Galaxy. Particular attention must be given to possible isotropic contributions from any of these foreground sources.

This paper summarizes the results of the DIRBE in-

vestigation, in which a direct measurement of the CIB has been made by measuring the absolute sky brightness at ten infrared wavelengths and searching for isotropic radiation arising outside of the solar system and Galaxy. We report upper limits on the CIB from 1.25 to 100 μm , and detection of the CIB at 140 and 240 μm . Section 2 briefly describes the DIRBE instrument and the character of its data. Section 2 also summarizes the procedures used to model foreground radiations, and for estimating the random and systematic uncertainties in the measurements and the models. Because the foreground models are critical to our conclusions, they are also described more extensively in separate papers. Details of the interplanetary dust (IPD) model used to discriminate the sky brightness contributed by dust in the solar system are provided by Kelsall et al. (1998, hereafter Paper II). Arendt et al. (1998, hereafter Paper III) describe the Galactic foreground discrimination procedures and summarize systematic errors in the foreground determination process. Section 3 of this paper summarizes the observational results, presented in compact form in Table 2. Dwek et al. (1998, hereafter Paper IV) show in detail that the isotropic residuals detected at 140 and 240 μm are not likely to arise from unmodeled solar system or Galactic sources. Section 4 of this paper summarizes that analysis, provides a comparison of the DIRBE results with other diffuse brightness and integrated discrete source measurements, presents limits on the integrated energy in the cosmic infrared background implied by the DIRBE measurements, and briefly discusses the implications of these results for models of cosmic evolution. A more extensive discussion of the implications is provided in Paper IV. Independent confirmation of the DIRBE observational results and extension of the CIB detection to longer wavelengths is provided by Fixsen et al. (1998), as discussed in § 4.2.1. The remainder of this Section provides an overview of the rather extensive arguments presented in this paper as a guide to the reader.

From absolute brightness maps of the entire sky over ten months of observation, the faintest measured value at each wavelength is determined (§ 3.1 and Table 2). These “dark sky” values are either direct measurements of the CIB (if we were fortuitously located in the Universe), or yield conservative upper limits on it. Since the measured infrared sky brightness is not isotropic at any wavelength in the DIRBE range, it cannot be concluded that these dark sky values are direct detections of the CIB. As expected, the dark sky values are least near 3.5 μm , in the relative minimum between scattering of sunlight by interplanetary dust and re-emission of absorbed sunlight by the same dust, and at the longest DIRBE wavelength, 240 μm , where emission from interstellar

dust is decreasing from its peak at shorter wavelengths and the cosmic microwave background has not yet become significant.

To proceed further, the contributions from the solar system and Galaxy to the DIRBE maps are determined. The contribution of interplanetary dust is recognizable because motion of the Earth in its orbit through this cloud causes annual variation of the sky brightness in all directions. An empirical, parametric model of the IPD cloud (§ 2.3 and Paper II) is used to extract the IPD contribution. Though this model is not unique, Paper II demonstrates that the implications for the CIB are reasonably robust, that is, rather insensitive to variations in the model.

The Galactic contribution from discrete sources bright enough to be detected individually is simply deleted from further analysis by blanking a small surrounding region in the maps. The integrated contributions of faint discrete Galactic sources are calculated at each wavelength from 1.25 to 25 μm from a detailed statistical model of Galactic sources and their spatial distribution (§ 2.3 and Paper III). The contribution from the diffuse interstellar medium (ISM) at each wavelength is obtained by scaling a template map of ISM emission to that wavelength. At all wavelengths except 100 μm , the template is the residual 100 μm map after removal of the IPD contribution, a map where ISM emission is prominent. To remove the ISM contribution without removing some fraction of the CIB at other wavelengths, the 100 μm extragalactic light is first estimated by extrapolating the H I – 100 μm correlation to zero H I column density for two fields, the Lockman hole (Lockman, Jahoda, & McCammon 1986) and north ecliptic pole, where there is known to be little other interstellar gas (molecular or ionized) in the line of sight (§ 3.4). This estimate is subtracted from the 100 μm map before scaling it to other wavelengths. The ISM template at 100 μm was chosen to be the map of H I emission, scaled by the slope of the H I-to-100 μm correlation (§ 2.3 and Paper III).

Clearly, drawing the proper conclusions from the DIRBE measurements and foreground models is critically dependent upon assessment of the uncertainties in both the measurements and the models. These uncertainties are discussed at length in Papers II and III, and are summarized here in § 2.4 and Table 2.

Because the foreground emissions are so bright, the definitive search for evidence of the CIB is carried out on the residual maps after removal of the solar system and Galactic foregrounds in a restricted region of the sky at high galactic and ecliptic latitudes (designated the “high quality” region B, HQB, discussed in § 3.3 and defined in Table 3). The HQB region is the largest area in which the residual maps do not clearly contain

artifacts from the foreground removal, and covers about 2% of the sky. It includes regions in both the northern and southern hemispheres and allows isotropy testing on 8,140 map pixels over angular scales up to 43 degrees within each hemisphere and from 137 to 180 degrees between hemispheres. In this region, the mean residuals are determined and their uncertainties are estimated. More precise estimates of the mean residuals at 100, 140 and 240 μm are obtained from a weighted average of values determined in the HQB region and in well-studied faint regions toward the Lockman hole and the north ecliptic pole. The residuals are tested for significance by requiring that they exceed three times the estimated uncertainty including both random and systematic effects.

The final step toward recognition of the CIB is to test for isotropy of the residuals. Though a number of approaches are discussed (§ 3.5), the conclusions are finally based upon the absence of significant spatial correlations of the residuals with any of the foreground models or with galactic or ecliptic latitude and the absence of significant structure in the 2-point correlation function in the HQB region.

Only at 140 and 240 μm do the results meet our two necessary criteria for CIB detection: significant residual in excess of 3σ and isotropy in the HQB region (§ 3.6). These isotropic residuals are unlikely to arise from unmodeled solar system or Galactic sources (§ 4.1 and Paper IV), leading to the conclusion that the CIB has been detected at 140 and 240 μm . At each wavelength shorter than 100 μm , an upper limit to the CIB is set at 2σ above the mean HQB residual, which in all cases is a more restrictive limit than the dark sky limit. At 100 μm , the most restrictive limit is found from the weighted average of the residuals in the HQB region, the Lockman hole and the north ecliptic pole. The last line of Table 2 shows the final CIB limits and detected values.

2. DIRBE, DATA, AND PROCEDURES

This section provides a brief review of the important features of the DIRBE instrument, the data it provides, and our reduction of the data with the goal of extracting the CIB. These topics are more thoroughly described in the *COBE*/DIRBE Explanatory Supplement (1997), and Papers II and III.

2.1. DIRBE Instrument Description

The *COBE* Diffuse Infrared Background Experiment was the first satellite instrument designed specifically to carry out a systematic search for the CIB in the 1.25–240 μm range. A detailed description of the *COBE* mission has been given by Boggess et al. (1992), and the DIRBE instrument has been described by Silverberg et

al. (1993). The DIRBE observational approach was to obtain absolute brightness maps of the full sky in 10 broad photometric bands at 1.25, 2.2, 3.5, 4.9, 12, 25, 60, 100, 140, and 240 μm . Table 1 summarizes the instrumental parameters, including the effective band width, beam solid angle, detector type, and filter construction. Though linear polarization was also measured at 1.25, 2.2, and 3.5 μm , the polarization information has not been used in this analysis.

DIRBE characteristics of particular relevance to the CIB search include:

(a) Highly redundant sky coverage over a range of elongation angles. Because the diffuse infrared brightness of the entire sky varies as a result of our motion within the IPD cloud (and possible variations of the cloud itself), the DIRBE was designed to scan half the sky every day, providing detailed “light curves” with hundreds of samples over the mission for every pixel. This sampling provides a strong means of discriminating solar system emission. The scanning was produced by offsetting the DIRBE line-of-sight by 30° from the *COBE* spin axis, which was normally fixed at a solar elongation angle of 94° , providing sampling at elongation angles ranging from 64° to 124° . Such sampling also modulates the signal from any nearby spherically symmetric Sun-or Earth-centered IPD component, which would otherwise appear as a constant (i.e., “isotropic”) signal.

(b) Sensitivity. Table 2 lists one-sigma instrumental sensitivities, $\sigma(\nu I_\nu)$, for each 0.7×0.7 field of view over the complete 10 months of cryogenic operation. These single field-of-view values are generally below the ac-

tual sky brightness, and below many of the predictions for the CIB. Averaging over substantial sky areas, once foregrounds are removed, increases the sensitivity for an isotropic signal.

(c) Stray light rejection. The DIRBE optical configuration (Magner 1987) was carefully designed for strong rejection of stray light from the Sun, Earth limb, Moon or other off-axis celestial radiation, as well as radiation from other parts of the *COBE* payload (Evans 1983). Extrapolations of the off-axis response to the Moon indicate that stray light contamination for a single field-of-view in faint regions of the sky does not exceed $1 \text{ nW m}^{-2} \text{ sr}^{-1}$ at any wavelength (*COBE/DIRBE* Explanatory Supplement 1997).

(d) Instrumental offsets. The instrument, which was maintained at a temperature below 2 K within the *COBE* superfluid helium dewar, measured absolute brightness by chopping between the sky signal and a zero-flux internal reference at 32 Hz. Instrumental offsets were measured about five times per orbit by closing a cold shutter located at the prime focus. A radiative offset signal in the long wavelength detectors arising from JFETs (operating at about 70 K) used to amplify the detector signals was identified and measured in this fashion and removed from the DIRBE data. Because the offset signal was stable over the course of the mission, it would appear as an isotropic signal if left uncorrected. To establish the origin of the radiative offset signal, and determine whether its value was the same whether the instrument shutter was closed (when the offset was monitored) or open (when the sky brightness plus offset was measured), special tests were conducted

TABLE 1
DIRBE INSTRUMENT CHARACTERISTICS

Band	λ^a (μm)	$\Delta\nu_e^b$ (Hz)	Beam Solid Angle (10^{-4} sr)	Detector Type	Filter Construction ^c	Absolute Calibration Reference Source
1	1.25 ^d	5.95×10^{13}	1.198	InSb ^e	Coated Glass	Sirius
2	2.2 ^d	2.24×10^{13}	1.420	InSb ^e	Coated Glass	Sirius
3	3.5 ^d	2.20×10^{13}	1.285	InSb ^e	Coated Germanium	Sirius
4	4.9	8.19×10^{12}	1.463	InSb ^e	MLIF/Germanium	Sirius
5	12	1.33×10^{13}	1.427	Si:Ga BIB	MLIF/Germanium/ZnSe	Sirius
6	25	4.13×10^{12}	1.456	Si:Ga BIB	MLIF/Silicon	NGC 7027
7	60	2.32×10^{12}	1.512	Ge:Ga	MLIF/Sapphire/KRS5/Crystal Quartz	Uranus
8	100	9.74×10^{11}	1.425	Ge:Ga	MLIF/KCl/CaF ₂ /Sapphire	Uranus
9	140	6.05×10^{11}	1.385	Si/diamond bolometer	Sapphire/Mesh Grids/BaF ₂ /KBr	Jupiter
10	240	4.95×10^{11}	1.323	Si/diamond bolometer	Sapphire/Grids/BaF ₂ /CsI/AgCl	Jupiter

^a Nominal wavelength of DIRBE band.

^b Effective bandwidth assuming source spectrum $\nu I_\nu = \text{constant}$.

^c MLIF = multi-layer interference filter.

^d Linear polarization and total intensity measured.

^e Anti-reflection coated for the band center wavelength.

during two one-week periods of the mission. In these tests, power to individual JFETs was turned off sequentially while measuring the offset (shutter closed) and sky brightness (shutter open) with all remaining operating detectors. The sky brightness measurements at each wavelength with JFETs off and on at other wavelengths were carefully compared. The offsets measured in this fashion were consistent with those measured by closing the shutter in normal operations, demonstrating that changing the position of the shutter did not significantly modify the offset. The final uncertainties in the offset corrections, shown as $S(\text{offset})$ in Table 2, are dominated by the uncertainties in the results of these special tests, due to the limited amount of time devoted to them. The uncertainties are quite negligible at wavelengths less than $140 \mu\text{m}$. The accuracy of the DIRBE measurement zero point at 140 and $240 \mu\text{m}$, where the offset uncertainty exceeds $1 \text{ nW m}^{-2} \text{ sr}^{-1}$, has been independently confirmed by comparison with *COBE*/FIRAS data, as discussed below.

(e) Gain stability. Short-term stability and linearity of the instrument response were monitored using internal radiative reference sources which were used to stimulate all detectors each time the shutter was closed. The highly redundant sky sampling allowed the use of stable celestial sources to provide precise photometric closure over the sky and reproducible photometry to $\sim 1\%$ or better for the duration of the mission.

(f) Absolute gain calibration. Calibration of the DIRBE photometric scale was obtained from observations of a few isolated bright celestial sources (*COBE*/DIRBE Explanatory Supplement 1997). Table 1 lists the DIRBE gain reference sources, and Table 2 lists the uncertainties in the absolute gain, $S(\text{gain})$, for each DIRBE spectral band.

An independent check of the DIRBE offset and absolute gain calibrations at 100 , 140 and $240 \mu\text{m}$ has been performed by Fixsen et al. (1997) using data taken concurrently by the FIRAS instrument on board *COBE*. The FIRAS calibration is intrinsically more accurate than that of the DIRBE, but the FIRAS sensitivity drops rapidly at wavelengths shorter than $200 \mu\text{m}$, effectively only partially covering the DIRBE $100 \mu\text{m}$ bandpass. In general, the two independent calibrations are consistent within the estimated DIRBE uncertainties. Quantitatively, Fixsen et al. evaluated the gain and offset corrections needed to bring the two sets of measurements into agreement. Taking account of the absolute FIRAS calibration uncertainty and the uncertainty arising from the comparison process itself (due in part to the need to integrate the FIRAS data over the broad DIRBE spectral response in each band and to integrate the DIRBE data over the large FIRAS beam

shape to obtain comparable maps), Fixsen et al. (1997) found statistically significant, but small, corrections (3σ or greater) to the DIRBE calibration only at $240 \mu\text{m}$. All results in this paper are based upon the DIRBE calibration and its uncertainties. The small effect of adopting the FIRAS calibration at 140 and $240 \mu\text{m}$, which has no qualitative effect on the conclusions presented here, is discussed in § 4.2.1.

2.2. The DIRBE Data

The calibrated DIRBE photometric observations are made into maps of the sky by binning each sample into a pixel on the *COBE* sky cube projection in geocentric ecliptic coordinates (*COBE*/DIRBE Explanatory Supplement 1997). The projection is nearly equal-area and avoids geometrical distortions at the poles. Pixels are roughly $20'$ on a side. Forty-one Weekly Maps have been produced by forming a robust average of all observations of each pixel taken during a week. About one-half of the sky is covered each week; complete sky coverage is achieved within four months. Data used in this analysis originate from the Weekly Sky Maps produced by the 1996 Pass 3b DIRBE pipeline software, as documented in the *COBE*/DIRBE Explanatory Supplement (1997).

All analysis is performed on maps in the original sky-cube coordinate system. For illustrational purposes, the maps shown in Figure 1 of this paper are reprojected into an azimuthal equal-area projection. The DIRBE surface brightness maps are stored as I_ν in units of MJy sr^{-1} . Many of the results in this paper are presented as νI_ν , where $\nu I_\nu (\text{nW m}^{-2} \text{ sr}^{-1}) = (3000 \mu\text{m}/\lambda) I_\nu (\text{MJy sr}^{-1})$.

2.3. Foreground Removal Procedures

Conservative upper limits on the CIB are easily determined from the minimum sky signal observed at each wavelength; these results are quoted in § 3.1. In order to derive more interesting limits or detections, one must address the problem of discriminating the various contributions to the measured sky brightness. The procedures used to discriminate and remove foreground emissions from the solar system and Galaxy are carefully based on distinguishing observational characteristics of these sources. Isotropy of the residuals was not assumed or imposed, but was rigorously tested (§ 3.5).

The approach adopted here is to derive, for each DIRBE wavelength, λ , an all-sky map of the residual intensity I_{res} remaining after the removal of solar-system and Galactic foregrounds from the observed sky brightness I_{obs} :

$$I_{res}(l, b, \lambda) = I_{obs}(l, b, \lambda, t) - Z(l, b, \lambda, t) - G(l, b, \lambda), \quad (1)$$

where l and b are galactic longitude and latitude, t is

TABLE 2
RESULTS OF THE DIRBE SEARCH FOR THE CIB

Wavelength (μm)	1.25	2.2	3.5	4.9	12	25	60	100	140	240	240 (ISM2)
$\sigma(\nu I_\nu)$	2.4	1.6	0.9	0.8	0.9	0.9	0.9	0.5	32.8	10.7	10.7
$S(\text{gain})$	3.1%	3.1%	3.1%	3.0%	5.1%	15.1%	10.4%	13.5%	10.6%	11.6%	11.6%
$S(\text{offset})$	0.05	0.028	0.015	0.010	0.015	0.010	1.34	0.81	5	2	2
$\nu I_\nu(\text{dark})$	374 ± 12	143 ± 4	60 ± 2	183 ± 5	2520 ± 129	2160 ± 330	261 ± 27	74 ± 10	57 ± 8	22 ± 3	22 ± 3
$\nu I_0(\text{NEP})$	40(3.0)(18)	6(1.3)(11)	6(0.7)(6)	16(0.3)(7)	125(0.3)(89)	145(0.2)(98)	30(0.2)(17)	21(0.3)(8)	16(1.4)(12)	7.2(0.5)(5)	22(1.3)(12)
$\nu I_0(\text{SEP})$	-9.2(6.4)(18)	-5.7(3.0)(11)	-2.4(1.1)(6)	16(0.6)(7)	112(0.4)(88)	122(0.2)(98)	21(0.1)(17)	...	37(2.6)(12)	20(0.8)(5)	16(2.4)(12)
$\nu I_0(\text{NGP})$	42(2.1)(21)	21(0.9)(12)	15(0.5)(6)	32(0.2)(8)	261(0.4)(138)	247(0.2)(156)	24(0.1)(27)	29(0.2)(10)	11(1.8)(12)	5.5(0.6)(5)	17(1.7)(12)
$\nu I_0(\text{SGP})$	36(2.3)(20)	19(0.9)(11)	16(0.5)(6)	36(0.3)(8)	255(0.5)(128)	232(0.3)(145)	22(0.1)(25)	24(0.2)(9)	7.0(1.9)(12)	4.5(0.6)(5)	20(1.8)(12)
$\nu I_0(\text{LH})$	69(5.9)(19)	26(2.4)(11)	16(1.1)(6)	30(0.6)(7)	208(0.3)(102)	215(0.3)(112)	24(0.1)(19)	23(0.2)(9)	18(3.4)(12)	11(1.0)(5)	14(3.2)(12)
$\nu I_0(\text{HQA})$	33(0.5)(21)	13(0.2)(12)	11(0.1)(6)	26(0.1)(8)	195(0.2)(138)	192(0.2)(156)	22(0.1)(27)	21(0.1)(10)	19(0.3)(12)	9.4(0.1)(5)	16(0.3)(12)
$\nu I_0(\text{HQB})$	33.0(1.6)(21)	14.9(0.6)(12)	11.4(0.4)(6)	24.8(0.2)(8)	192(0.2)(138)	192(0.2)(156)	20.6(0.1)(27)	19.0(0.1)(9.5)	18.5(0.5)(12.0)	9.7(0.2)(5.2)	13.8(0.5)(12)
$\nu I_0(\text{LH}'\text{,HI})$	22.3(0.2)(6.1)	26.6(0.9)(7.3)	13.9(0.3)(2.6)	...
$\nu I_0(\text{NEP}'\text{,HI})$	17.3(0.4)(6.3)	23.1(1.9)(13.2)	14.3(0.6)(4.5)	...
$\partial_b \nu I_0(\text{HQB})$	67.2 ± 25.0	1.4 ± 10.9	-19.5 ± 5.3	-33.4 ± 2.7	-159 ± 3.6	-115 ± 4.4	1.1 ± 0.9	-26.0 ± 1.9	3.2 ± 15.4	2.2 ± 5.1	6.6 ± 14.6
$\partial_\beta \nu I_0(\text{HQB})$	-9.3 ± 11.5	3.9 ± 5.0	15.3 ± 2.5	20.9 ± 1.3	104 ± 1.5	83.3 ± 1.9	-0.8 ± 0.4	19.4 ± 0.9	-9.5 ± 7.2	-3.5 ± 2.4	3.6 ± 6.9
νI_0 (95% CL)	< 75	< 39	< 23	< 41	< 468	< 504	< 75	< 38	< 43	< 20	< 28
$\langle \nu I_0 \rangle$	21.9 \pm 6.1	25.0 \pm 6.9	13.6 \pm 2.5	...
Isotropy	no	no	no	no	no	no	no	no	yes	yes	yes
CIB	< 75	< 39	< 23	< 41	< 468	< 504	< 75	< 34	25.0 \pm 6.9	13.6 \pm 2.5	...

NOTE.—Subscript 0 means residual. Results are in units of $\text{nW m}^{-2} \text{sr}^{-1}$. Row 1: nominal wavelength of the DIRBE photometric bands. The last column presents results at 240 μm using the two-component ISM model. Row 2: mission-averaged 1σ instrument sensitivity per $0^\circ 7 \times 0^\circ 7$ field-of-view. Row 3: percent uncertainty in the absolute gain calibration. Row 4: uncertainty in the instrumental offset (zero point) calibration. Row 5: minimum observed sky brightness. Errors are estimated from the quadrature sum of the gain and offset uncertainties. Rows 6 – 10: residual intensity derived using the 100 μm map as a template for the ISM at small patches toward the north (NEP) and south (SEP) ecliptic poles, the north (NGP) and south (SGP) galactic poles, and the Lockman hole (LH). The 100 μm column shows residuals using the Bell Labs H I map as the ISM template. Final column shows results using the 2-component (100 and 140 μm) ISM template. Random (systematic) 1σ errors are shown in the first (second) parentheses. Rows 11 – 12: residual intensity derived using the 100 μm map as a template for the ISM (Bell Labs H I template in the 100 μm column and 2-component template in the last column) at the “high quality” HQA and HQB regions defined in Table 3 in units of $\text{nW m}^{-2} \text{sr}^{-1}$. Random (systematic) 1σ errors are shown in the first (second) parentheses. Rows 13 – 14: residual intensity derived from the H I correlation at the Lockman hole (LH) and the north ecliptic pole (NEP). Random errors (systematic errors) are shown in the first (second) parentheses. Rows 15 – 16: spatial gradients of the residual intensities in the HQB region with respect to $\csc |b|$ and $\csc |\beta|$. Row 17: 2σ upper limit on the CIB, derived from the HQB region using random and systematic uncertainties combined in quadrature. The 240 (ISM2) entry is derived from the dark sky value, since it yields a more restrictive limit. Row 18: weighted average of the residuals at the HQB region, the Lockman hole, and the north ecliptic pole (rows 12, 13, & 14), weighted by the quadrature sum of the random and non-common mode systematic errors in each region. Errors in the mean include the random and all systematic errors. Row 19: result of the 2-point correlation function isotropy test of the residual intensities in the HQB region: no = not consistent with isotropy; yes = consistent with isotropy. Row 20: DIRBE detections of the CIB or 95% confidence upper limits.

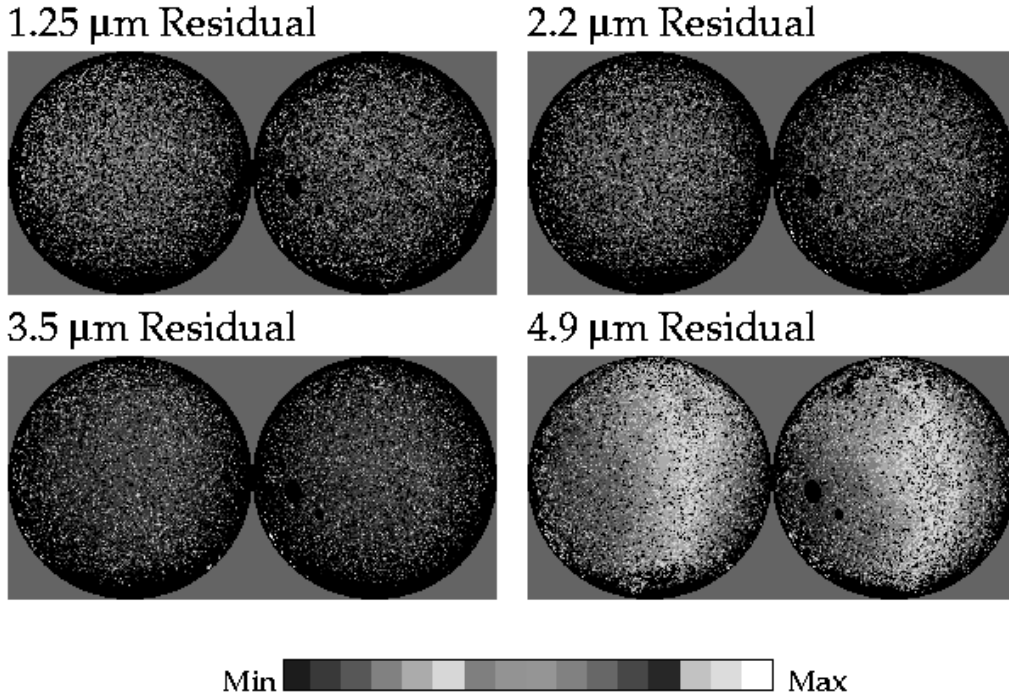


Fig. 1.—DIRBE residual intensity maps after removal of foreground emission at 1.25 – 240 μm , shown in galactic coordinates with an azimuthal equal-area projection. The left (right) circle represents the projected north (south) Galactic hemisphere with $b = +90^\circ$ ($b = -90^\circ$) in the center and $b = 0^\circ$ at the edge. Contours of fixed latitude are concentric circles with $r \propto [(1 - \sin |b|)/2]$. Longitude lines run radially from the pole to the edge and increase clockwise (counterclockwise) on the left (right) hemisphere. The longitude $l = 0^\circ$ runs from the center to the bottom edge of each projected hemisphere. All maps are plotted on a linear scale with color-coded brightness ranges of $(-0.05, 0.3)$, $(-0.05, 0.3)$, $(-0.01, 0.2)$, $(0, 0.2)$, $(0, 2)$, $(0.5, 3)$, $(0, 3)$, $(0, 15)$, $(0, 20)$, and $(0, 20)$ in units of MJy sr^{-1} . Values below (above) the plot range are shown in black (white).

time, $Z(l, b, \lambda, t)$ is the contribution from the interplanetary dust cloud, and $G(l, b, \lambda)$ is the contribution from both stellar and interstellar dust components within the Galaxy. Both Z and G are derived from models. The choice of models is motivated by the primary goal of ensuring that no part of the CIB is inadvertently included in the interplanetary dust cloud or Galactic emission components. Figure 1 presents maps of I_{res} as derived from the foreground removal process.

The DIRBE IPD model (Paper II) is a semi-physical, parametric model of the sky brightness similar, but not identical, to that used to create the *IRAS* Sky Survey Atlas (Wheelock et al. 1994). The model represents the sky brightness as the integral along the line-of-sight of the product of an emissivity function and

a three-dimensional dust density distribution function. The emissivity function includes both thermal emission and scattering. The thermal emission at each location assumes a single dust temperature for all cloud components. The temperature is a function only of distance from the Sun and varies inversely as a power law with distance. The density distribution includes a smooth cloud, three pairs of asteroidal dust bands, and a circumsolar dust ring. The model is intrinsically static, except that structure within the circumsolar ring near 1 AU is assumed to co-orbit the Sun with the Earth. The apparent seasonal brightness variation arises from the motion of the Earth on an eccentric orbit within the cloud, which is not required to be symmetric with respect to the ecliptic plane.

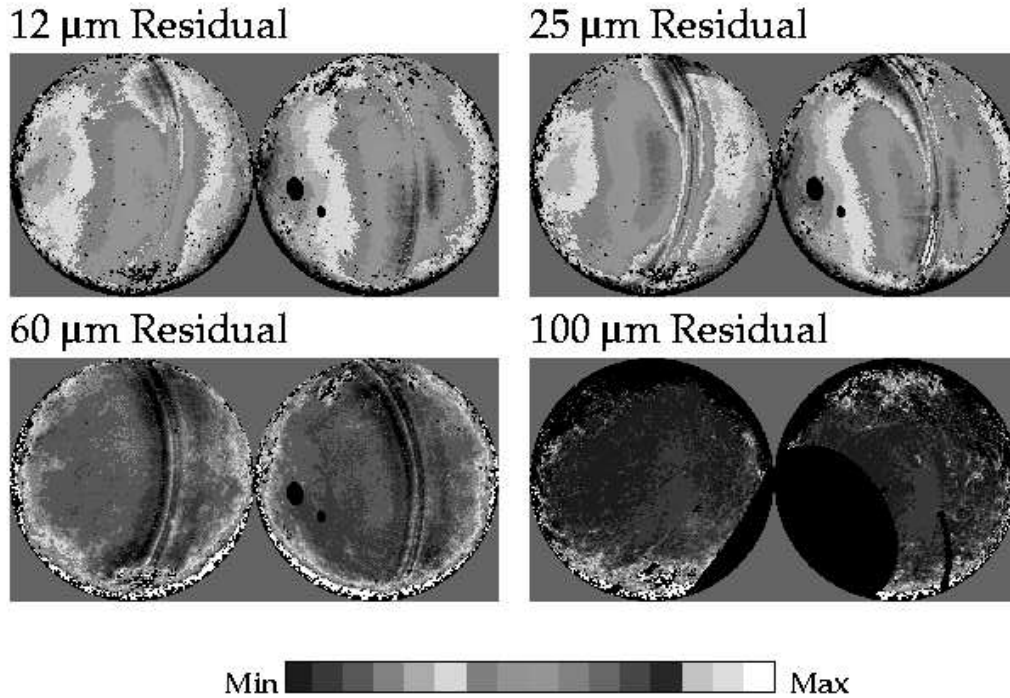


Fig. 1.—continued.

Analytical forms are assumed for the density distributions, scattering phase function, and thermal emission characteristics of the dust. Parameters for the analytical functions are determined by optimizing the model to match the observed temporal variations in brightness toward a grid of directions over the sky. By fitting only the observed time variation to determine the model parameters, Galactic and extragalactic components of the measured brightness are totally excluded. However, it must be emphasized that this method can not uniquely determine the true IPD signal; in particular, an arbitrary isotropic component could be added to the model without affecting the parameter values determined in our fitting to the seasonal variation of the signal. No such arbitrary constants are added to the brightnesses obtained directly from our model, and limits on unmodeled isotropic components of the IPD cloud emission are set based upon independent knowledge of the nature of the cloud (§ 4.1). Once the optimal model parameters are determined, the IPD model is integrated along the line of sight to evaluate Z at the mean time of observation of each DIRBE pixel for each week of the mission.

The calculated IPD map is then subtracted from each DIRBE Weekly Map and an average mission residual computed. This simple model represents the IPD signal fairly well, but there are clearly systematic artifacts in the residuals at the level of a few percent of the IPD model brightness (Paper II). Because the zodiacal emission is so bright, uncertainties in the residual sky maps at 12–60 μm are dominated by the uncertainties in the IPD signal.

The Galactic model G is removed from the mission-averaged residuals formed after removal of the IPD contribution (Paper III). The Galactic model actually consists of three separate components: bright discrete sources, faint discrete sources, and the interstellar medium. Both stellar and extended discrete sources whose intensity above the local background exceeded a wavelength-dependent threshold are excluded by blanking a small surrounding region from each of the ten maps. The blanked regions appear black in Figure 1, and are most evident in the 1.25–4.9 μm maps and at low galactic latitude. The contribution from faint discrete sources below the bright-source blanking

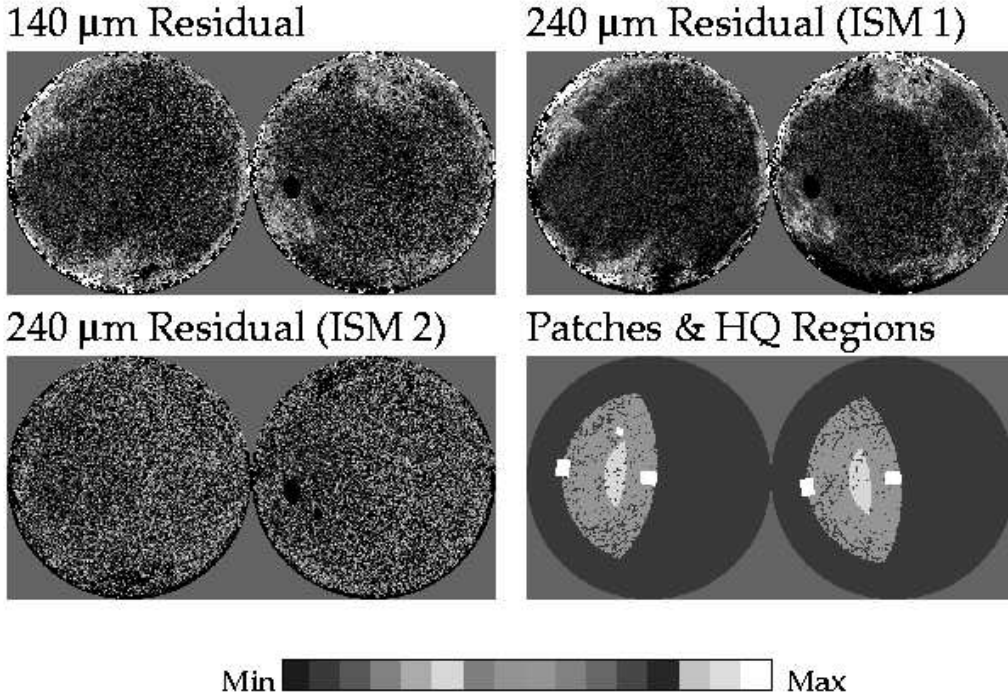


Fig. 1.—continued. The last panel indicates the sky locations of the five small patches (§ 3.2) and the two selected high quality regions (§ 3.3): the tiny white square in the left hemisphere is the Lockman hole, the centered white square in the left (right) hemisphere is the north (south) Galactic pole, and the remaining white square in the left (right) hemisphere is the north (south) ecliptic pole; the large grey area in the left (right) sphere is the north (south) high quality region A, and the small light grey area in the left (right) hemisphere is the north (south) high quality region B.

threshold at $1.25 - 25 \mu\text{m}$ is then removed by subtracting the integrated light from a statistical source-count model based on that of Wainscoat et al. (1992), with elaborations by Cohen (1993, 1994, 1995). We call this the faint source model (FSM). The use of a source-count based model ensures that the related intensity represents only Galactic sources. The stellar contribution is neglected at wavelengths longward of $25 \mu\text{m}$.

The basic model of emission from interstellar dust, $G_I(l, b, \lambda)$, consists of a standard spatial (wavelength-independent) template of the brightness of the interstellar medium (ISM), scaled by a single factor $R(\lambda)$ at each wavelength. The factor $R(\lambda)$ is determined by the slope of a linear correlation of the standard spatial template with the intermediate residual map at wavelength λ obtained from the measured map, $I_{obs}(l, b, \lambda, t)$, by subtraction of the IPD model, blanking of bright sources,

and subtraction of the FSM. The ISM spatial template is constructed so that it does not contain diffuse extragalactic emission. To the extent that this is successful, when the scaled ISM template at any wavelength, $G_I(l, b, \lambda)$, is subtracted from the intermediate residual map at that wavelength, any CIB signal in the resulting final residual map $I_{res}(l, b, \lambda)$ is not modified. This linear ISM model works well in that it removes the evident cirrus clouds, especially in the high galactic latitude regions where the search for the CIB is conducted.

Several approaches have been used to create the ISM spatial template. In one approach, the $100 \mu\text{m}$ ISM map, $G_I(l, b, 100 \mu\text{m})$, obtained by subtracting the contributions from the IPD and bright and faint discrete Galactic sources from the observed map at $100 \mu\text{m}$, was used as the spatial template for all other wavelengths from 12 to $240 \mu\text{m}$. No significant ISM emission could be iden-

tified at 1.25 and 2.2 μm , and a modified form of this procedure was required to detect the weak ISM emission at 3.5 and 4.9 μm (Paper III). The use of the 100 μm ISM emission as the template at other wavelengths has the advantages of good signal-to-noise ratio and an ideal match of angular resolution with the other DIRBE data. Furthermore, the use of an infrared map as the template automatically includes contributions from dust in all gas phases of the ISM. The procedure used to estimate the 100 μm CIB signal so as to remove it from the 100 μm ISM map is described briefly below and in § 3.4.

For additional analysis of the 240 μm map, a two-component model of the ISM emission (“ISM2”) was also generated. This model used a linear combination of the DIRBE 100 and 140 μm ISM maps as a template. While the one-component (100 μm) model (“ISM1”) appears to work adequately at high latitudes, where we could best test for isotropic residuals, the ISM2 model can account for spatial variations in dust temperature throughout the ISM (Paper III). This leads to a more accurate model of the ISM emission, particularly at low galactic latitudes, and a residual map $I_{res}(l, b, 240 \mu\text{m})$ that is more weakly correlated with the ISM template than in the case of the ISM1 model. Figure 1 shows maps of $I_{res}(l, b, \lambda)$ at 240 μm for both the ISM1 and ISM2 models.

To search for evidence of an isotropic CIB residual at 100 μm , an ISM spatial template independent of the measured 100 μm map was needed. For this purpose a velocity-integrated map of H I column density was used as the spatial template of the ISM emission. The range of velocities in the H I map was restricted so that it contained only Galactic H I emission. The success of this procedure of course depends on the accuracy with which the H I traces the dust distribution, at least at the high galactic latitudes of interest here. Paper III provides extensive discussion of the uncertainty in the correlation of infrared brightness with H I column density.

The H I spatial template used to remove ISM emission from the map at 100 μm was the Bell Labs H I survey (Stark et al. 1992). This survey has the advantages of a well-established baseline and large area coverage, but the disadvantage of lower angular resolution than the DIRBE data. Higher resolution H I data (Elvis, Lockman, & Fassnacht 1994; Snowden et al. 1994), obtained in small regions where there are observational constraints on the amount of molecular and ionized material (Paper III), and calibrated with the Bell Labs H I survey, were used to establish the scaling factor between the H I and 100 μm ISM emission. These same high resolution data were used to estimate the 100 μm brightness at zero H I column density so as to remove diffuse extragalactic emission from the ISM spatial template, $G_I(l, b, 100 \mu\text{m})$, used at all other wavelengths as

discussed above (see § 3.4).

The 100 μm – H I correlation was also evaluated using the new Leiden/Dwingeloo H I survey (Hartmann & Burton 1997), but this made little difference in the scaling factor or the residual intensity $I_{res}(l, b, 100 \mu\text{m})$. Use of the Leiden/Dwingeloo H I survey as the spatial template of the ISM at 100 μm produces a cleaner map of residual emission $I_{res}(l, b, 100 \mu\text{m})$ than does use of the Bell Labs data, because of a better match to the DIRBE angular resolution, but the differences are not very apparent in maps made in the projection and scale of those in Figure 1. Results quoted in this paper are based on the Bell Labs H I survey and other observations that are directly calibrated to that data set (Elvis, Lockman, & Fassnacht 1994; Snowden et al. 1994).

2.4. Uncertainties

For this analysis it is useful to make distinctions between three forms of uncertainties. First are the *random uncertainties* which include instrumental noise, uncorrected instrument gain variations, random fluctuations of the stellar distribution, and certain deficiencies in the foreground modelling procedures. The key property of random uncertainties is that they are reduced as one averages over longer time intervals or larger regions of the sky. Table 2 lists typical values for the detector noise per pixel averaged over the entire mission, $\sigma(\nu I_\nu)$, assuming 400 observations per pixel. The bolometer detectors used at 140 and 240 μm are distinctly less sensitive than the other detectors.

The second form of uncertainty is the *gain uncertainty*. This is the uncertainty in the gain factor used in the absolute calibration of the DIRBE data. While the gain uncertainty does affect the quoted intensities, including the residual intensities, in a systematic way, it does not alter the signal-to-noise ratio of the results or the detectability of an isotropic residual signal using our methods. We therefore distinguish the gain uncertainty, shown as $S(\text{gain})$ for each wavelength band in Table 2, from other systematic errors.

Finally there are the *systematic uncertainties*, which are the uncertainties in the data and the foreground models that tend to be isotropic or very large scale. The systematic uncertainties cannot be reduced by averaging, and therefore are the ultimate limitations in the detection of the CIB. Table 2 lists the detector offset uncertainties, $\sigma(\text{offset})$. The offset uncertainties are important contributors to the total uncertainty only at 140 and 240 μm . The systematic uncertainties of the IPD model, the stellar emission model, and the ISM model are important respectively at 1.25 – 100 μm , 1.25 – 4.9 μm , and 100 – 240 μm . Papers II and III discuss in detail the estimation of the systematic un-

certainties in the foreground models; Table 6 of Paper III lists the systematic uncertainty associated with each foreground. The systematic uncertainty in each residual shown in Table 2 of this paper is the quadrature sum of the individual contributions identified in Paper III. The total uncertainties used to state our most restrictive upper limits on the CIB, and the uncertainty in the CIB detections at 140 and 240 μm , are estimated as the quadrature sum of the random and systematic uncertainties. Table 2 of this paper and Table 6 of Paper III clearly show that *the total uncertainties are dominated by the systematic uncertainties in removing the foreground contributions to the infrared sky brightness.*

3. OBSERVATIONAL RESULTS

3.1. Dark Sky Limits

The most conservative direct observational limits on the CIB are derived from the minimum observed sky brightnesses. In each DIRBE weekly sky map, the faintest direction has been determined for each wavelength. At wavelengths where interplanetary dust scattering or emission is strong, the sky is darkest near the ecliptic poles. At wavelengths where the IPD signal is rather weak (i.e., longward of 100 μm), the sky is darkest near the galactic poles or in minima of H I column density. The smallest of these values at each wavelength over the duration of the mission is the “dark sky” value, listed in Table 2 as $\nu I_\nu(\text{dark})$. The uncertainty shown for each value is the quadrature sum of the contributions from the gain and offset 1σ uncertainties. We define “dark sky” upper limits to the CIB at the 95% confidence level (CL) as 2σ above the measured dark sky values.

3.2. Residuals in Small Dark Patches

After removing the contributions of interplanetary dust (Paper II), bright and faint discrete galactic sources, and the interstellar medium (Paper III) from the measured sky brightness, the residual signal at high galactic and ecliptic latitudes is positive and generally rather featureless, though low level artifacts from systematic errors in the models are clearly present. To illustrate the magnitude of the foreground signals, Figure 2 shows the DIRBE spectrum of the total observed sky brightness averaged over a $5^\circ \times 5^\circ$ region at the Lockman hole, the region of minimum H I column density at $(l, b) \sim (150^\circ, +53^\circ)$ [geocentric ecliptic coordinates $(\lambda, \beta) \sim (137^\circ, +45^\circ)$] (Lockman, Jahoda, & McCammon 1986; Jahoda, Lockman, & McCammon 1990). Figure 2 also shows the individual contributions from the foreground sources and the residuals after removing the foreground

contributions. Scattering and emission from the interplanetary dust dominates all other signals from 1.25 to 100 μm . This is true even at 3.5 μm , the spectral “window” between the maxima of the scattered and emitted IPD signal. Only at 140 and 240 μm does some other foreground signal, that from the interstellar medium (infrared cirrus), become dominant.

Some insight into the residuals is provided by looking at several high latitude regions (Hauser 1996a, b). For this purpose, we have examined the residuals in $10^\circ \times 10^\circ$ fields at the north and south Galactic and ecliptic poles (designated NGP, SGP, NEP, and SEP respectively), and a $5^\circ \times 5^\circ$ field in the Lockman hole (LH). Table 2 lists the mean residual brightnesses for these five patches after all of the foreground removal steps listed above. As discussed in § 2.3, the 100 μm map was used as the ISM template in producing the residual maps at all wavelengths except 100 μm . At 100 μm , the Bell Labs H I map was used as the ISM template. While the range of residual values at each wavelength is substantial, typically a factor of 2 or more, comparison with the dark sky values shows that these residuals are small fractions, approaching 10% at wavelengths shortward of 100 μm , of the dark sky values. However, the fact that the residuals are brightest in the region of peak IPD thermal emission, 12 to 25 μm , strongly suggests that significant foreground emission still remains, at least in the middle of the DIRBE spectral range. This is not surprising in view of the very apparent residual IPD modelling errors at these wavelengths (e.g., Fig. 1, especially 4.9 to 100 μm ; and Paper II).

3.3. Residuals in High Quality Regions

While each of the small dark patches (§ 3.2) is situated where one of the IPD, stellar, or ISM foregrounds is minimized, each patch is also located in a region where the other foregrounds may be strong. Therefore, we defined “high quality” (HQ) regions where all foregrounds are expected to be relatively weak. The range of ecliptic latitude, β , was restricted to exclude bright scattering and emission from the IPD, and the range of galactic latitude, b , was restricted to exclude regions with bright stellar emission. To avoid regions with bright ISM emission, locations where the 100 μm brightness, after the IPD contribution was removed, was more than 0.2 MJy sr^{-1} above the local mean level were also excluded. The largest region that can reasonably be considered as high quality covers $\sim 20\%$ of the sky between the Galactic and ecliptic poles and is designated HQA. A much more restrictive region, designated HQB, lies in the center of the HQA region and includes $\sim 2\%$ of the sky. Table 3 lists the constraints for the HQ regions, and the last panel of Figure 1 shows the areas covered by the HQ

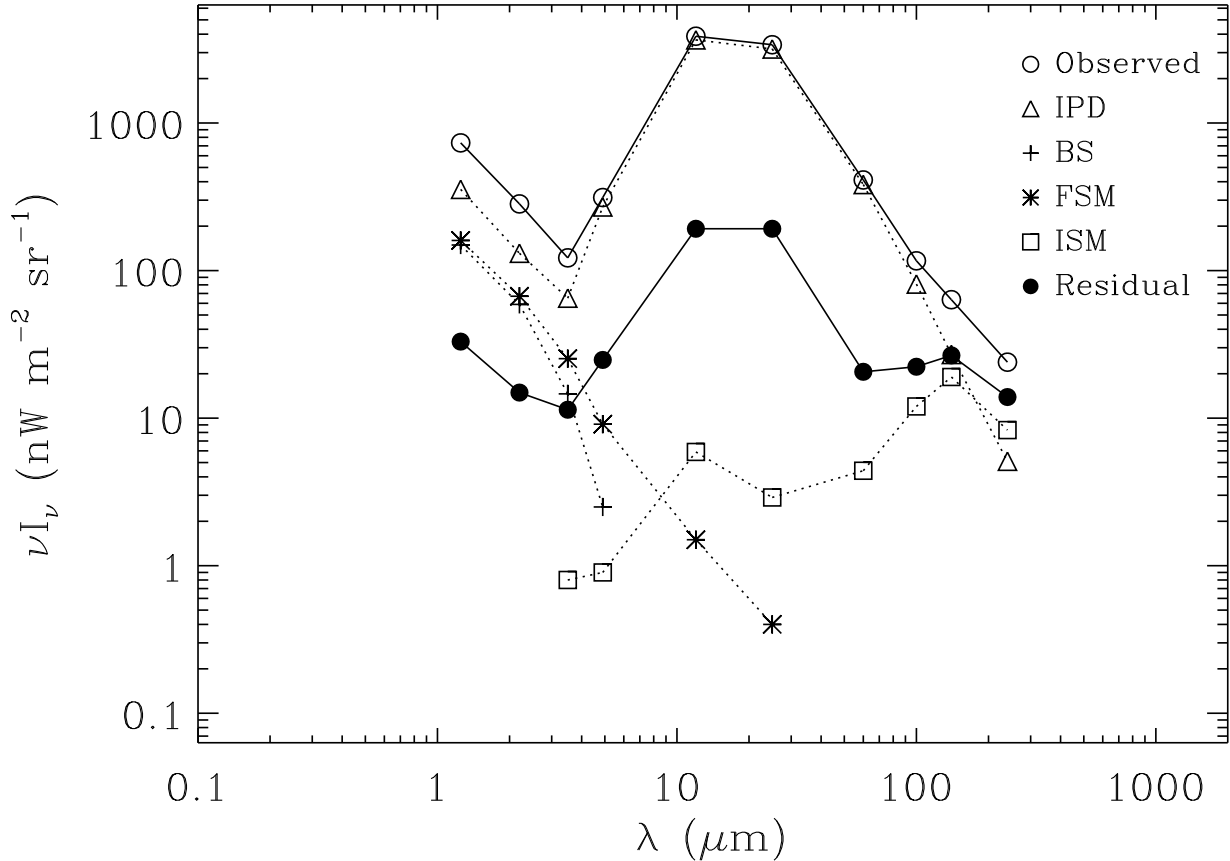


Fig. 2.—Contributions of foreground emission to the DIRBE data at 1.25 – 240 μm in the Lockman hole area: observed sky brightness (open circles), interplanetary dust (triangles), bright galactic sources (crosses), faint galactic sources (stars), and the interstellar medium (squares). Filled circles show the residual brightness after removing all foregrounds from the measurements.

regions. Each HQ region is composed of corresponding northern and southern segments.

Table 2 lists the mean residual intensities, $\nu I_0(\text{HQA})$ and $\nu I_0(\text{HQB})$, for the HQ regions after all foregrounds have been removed. As in the analysis of the small dark patches (§ 3.2), the 100 μm map was used as the ISM template in producing the residual maps at all wavelengths except 100 μm . At 100 μm , the Bell Labs H I map was used as the ISM template. The statistical uncertainty of the mean, which is calculated from the observed rms variation of the residual emission over the region, is also shown. For HQB, the total systematic uncertainty estimated for each band is also listed in Table 2. While some portions of the systematic uncertainty needed to be evaluated at regions other than the HQ regions (see Papers II and III), the numbers listed here should be appropriate for HQB. The systematic uncer-

tainties are larger when dealing with other areas where the foreground emission removed was stronger.

3.4. Residuals at the Lockman Hole and the North Ecliptic Pole

The intercept of a linear fit to the correlation between the infrared emission and the H I column density yields an estimate of the isotropic residual component of infrared emission. This technique was used (§ 2.3 and Paper III) to establish the amount of emission that needed to be removed to create the 100 μm template of the ISM. The H I data were from Snowden et al. (1994) for a 250 deg^2 region covering the Lockman hole (LH'), and from Elvis, Lockman, & Fassnacht (1994) for a 70 deg^2 region around the north ecliptic pole (NEP'). These regions are denoted with primes to distinguish them from the “dark patches” LH ($5^\circ \times 5^\circ$ patch) and NEP ($10^\circ \times 10^\circ$

patch) at similar locations but of somewhat different size discussed in § 3.2. Figures 7 and 8 of Paper III show that the 100 μm brightness and H I column density are linearly related at low column density in these regions. Within these regions, linear fits to the correlations between the 140 and 240 μm emission and the H I column density were also calculated. Table 2 lists the intercepts of these fits as $\nu I_0(\text{LH}', \text{HI})$ and $\nu I_0(\text{NEP}', \text{HI})$.

The advantage of this technique for estimating the CIB at 140 and 240 μm , over our standard method using the 100 μm data for the ISM template, is that the systematic uncertainties of the 100 μm data, including those caused by uncertainties in the 100 μm IPD model and in the extrapolation of the 100 μm —H I correlation to zero H I column density, are not propagated into the 140 and 240 μm results. Thus, the systematic uncertainties for $\nu I_0(\text{LH}', \text{HI})$ are smaller than those for $\nu I_0(\text{HQB})$. For the NEP region, the intercept of the correlation must be extrapolated over a longer interval of H I column density and from fewer data, so the systematic uncertainties for $\nu I_0(\text{NEP}', \text{HI})$ are only smaller than those of $\nu I_0(\text{HQB})$ at 100 μm .

A disadvantage of this technique is that the H I does not trace other phases of the ISM (ionized and molecular gas) that may also contribute to the observed infrared emission. Any part of the emission from other phases that is not directly correlated with the H I column density will appear as an additional contribution to $\nu I_0(\text{LH}', \text{HI})$ and $\nu I_0(\text{NEP}', \text{HI})$. Additionally, even within the neutral ISM, the assumed linear correlation between infrared brightness and H I column density cannot track large- or small-scale variations in the dust temperature or gas-to-dust mass ratio. This is apparent in the 100 μm residual map (Fig. 1), where the ISM emission is strongly oversubtracted in the outer Galaxy and undersubtracted in the inner Galaxy. Emission from numerous molecular clouds is also visible at high latitudes.

Because there are available data on all gas phases in the NEP' and LH' regions, it is possible to set tight limits on the uncertainty in the extrapolation of the infrared—H I correlation to zero H I column density in

these regions (Paper III). We estimate that dust in the ionized ISM uncorrelated with H I contributes less than $4 \text{ nW m}^{-2} \text{ sr}^{-1}$ to the 100 μm residual intensity. Assuming that the infrared spectrum of the ionized medium is the same as that of the neutral medium, the contributions from the ionized ISM at 140 and 240 μm are less than $5 \text{ nW m}^{-2} \text{ sr}^{-1}$ and $2 \text{ nW m}^{-2} \text{ sr}^{-1}$ respectively. If such large contributions were to exist, then the residual intensities listed in Table 2 would have to be reduced accordingly. Even in this case, the 240 μm result would still be a 3σ detection of residual emission.

Analysis in Paper III also shows that infrared emission from the molecular ISM is only poorly constrained by upper limits on CO observations. Constraints based on visual extinction measurements suggest the contribution from dust in the molecular ISM is negligible at 100 μm . Contributions at 140 and 240 μm should be similarly low.

3.5. Isotropy of the Residual Emission

The signature of the diffuse CIB is an isotropic signal. Several tests of the isotropy of our residual signals have therefore been performed. Fundamentally, each test checks whether the background intensities in different directions agree within the limit of the estimated uncertainties.

3.5.1. Mean Patch Brightnesses

The first test involves comparison of the mean brightnesses of the small dark patches discussed in § 3.2. For each patch the mean brightness and the standard deviation of the mean ($\nu I_0 \pm \sigma_m$) are listed as the residual value and random error in Table 2. Two patches whose means differ by less than $2\sigma_m(\text{total}) = 2\sqrt{\sigma_m(1)^2 + \sigma_m(2)^2}$ are consistent with isotropy between those regions of the sky. This is a strict constraint on isotropy, in that it does not allow for differences between patches that are larger than the random errors but within the systematic uncertainties.

Some pairs of patches pass this strict test for isotropy at 1.25, 2.2, 3.5, 4.9, 140 and 240 μm . For the ISM2

TABLE 3
HIGH QUALITY REGION DDEFINITIONS

Region	b limit	β limit	100 μm ISM	Area ^a		
			limit (MJy/sr)	(pixels)	(deg ²)	(sr)
HQA	> 30	> 25	< 0.2	83671	8780	2.67
HQB	> 60	> 45	< 0.2	8140	854	0.26

^a Bright source removal reduces these areas by up to 35% at near-IR wavelengths.

model (§ 2.3), the mean 240 μm residual intensity of each patch except the NEP is consistent with that of each of the other patches. However, in most cases the differences between the mean residuals of the patches are larger than expected for purely random noise in measurements of an isotropic residual. At mid-infrared wavelengths, the systematic effect of the residual IPD emission is evident in that the north and south ecliptic pole patches are at nearly the same brightness, while the lower ecliptic latitude patches at the Galactic poles are significantly brighter.

If the criterion for isotropy is taken to be agreement within the systematic uncertainties, which are also shown in Table 2, then most pairs of patches pass the test at all wavelengths. Exceptions are that intensities at the Galactic poles tend to differ from those at the ecliptic poles at wavelengths where the IPD emission is strong, and the residual intensity in the SEP patch is anomalously low in the near-infrared and high in the far-infrared.

A test for equal mean intensities was also applied for the north and south halves of the HQB region. In this case, the confidence levels of the equality were determined through the bootstrap method and the t -statistic of the Fisher-Behrens test:

$$t = \frac{\bar{N} - \bar{S}}{\sqrt{\sigma_N^2/n_N + \sigma_S^2/n_S}}, \quad (2)$$

where \bar{N} and \bar{S} are the mean intensities over n_N and n_S pixels in the north and south halves of the HQB region. Only at 3.5 μm and 240 μm were the two means plausibly equal, to significance levels of 36% and 75% respectively. At the other wavelengths, the highest significance level of equality was only 0.3% (at 140 μm).

3.5.2. Brightness Distributions

The next set of isotropy tests involves checking whether the dispersion in brightness for pixels in an area is consistent with the dispersion due to the known random uncertainties. If the data show no variation in excess of that expected from the random uncertainties then the patch is said to be isotropic. This test gains statistical significance when large patches are used. We applied this test in the HQ regions defined in § 3.3.

For wavelengths of 12 – 240 μm , the probability distributions for the intensity of each pixel were calculated assuming Gaussian dispersions of both ISM model errors (proportional to the ISM intensity) and a combination of detector noise and IPD model errors (measured at each pixel as the standard deviation of the weekly map intensities, after removal of IPD emission). The random uncertainties of the stellar model are included as an additional Gaussian component to the dispersion at 12 and

25 μm , even though the contribution from stars is small enough that this additional term is minor. The expected intensity distribution for the entire patch is then constructed from the sum of these Gaussian distributions over all pixels.

For wavelengths of 1.25 – 4.9 μm , the residual fluctuations from faint sources dominate the variations within the HQ regions. For these wavelengths and for each HQ region, the faint source model (§ 2.3) was used to generate random samples of pixel brightnesses using Poisson statistics. We then added random Gaussian errors corresponding to the combined detector noise and IPD model uncertainties, and the ISM uncertainties at wavelengths for which the ISM was modeled (3.5 and 4.9 μm).

For all wavelengths, the observed and expected residual brightness distributions were compared using the Kolmogorov-Smirnov (K-S) test. At wavelengths greater than 12 μm the χ^2 test was also applied. These statistics indicate isotropy for the 240 μm residuals in the HQA (ISM1) and HQB (ISM1 & ISM2) regions. The residuals in the HQB region are also found to be isotropic at 140 μm . The 60 and 100 μm intensity distributions fail the tests, despite their qualitatively similar observed and expected distributions. The 12 and 25 μm distributions fail the test badly, because of residual structure from imperfect removal of the IPD emission. At the near-infrared wavelengths, the FSM predicts slightly wider distributions than are observed.

This brightness distribution test moves beyond the simple comparison of mean intensities and can reveal the presence of unusually bright or dark features within a region. The main drawback of this test is that it lacks any sensitivity to the spatial distribution of the residual emission within a region.

3.5.3. Systematic Spatial Variations

An area where the residual intensity is isotropic will have no significant spatial variations or structure. The residual emission in the HQ regions has been tested for systematic variations by looking for linear correlations of the residual intensity with $\csc(|b|)$ and $\csc(|\beta|)$, and with the intensities of the IPD, faint source and ISM models. The slopes of these correlations indicate the gradients in the residual intensities with respect to each correlant. There were statistically significant slopes to all of these correlations in the HQA regions. These correlants are not all independent. Correlations with all of them can be produced by low-level artifacts due to imperfections in any one of the foreground models. Examination of the residual maps (Fig. 1) shows evident residuals from the IPD and ISM model removal in the HQA region, consistent with these formal tests. In the HQB regions, the residual emission at 140 and 240 μm did not exhibit

any significant correlations, even though the tests were sensitive enough to detect correlations as strong as those found in the larger HQA regions. At other wavelengths, correlations with at least one of the models were present. For HQB, the slopes of the correlations with respect to $\csc(|b|)$ and $\csc(|\beta|)$ and their statistical uncertainties are listed as $\partial_b \nu I_0(\text{HQB})$ and $\partial_\beta \nu I_0(\text{HQB})$ in Table 2. The high quality regions HQA and HQB were defined *a priori* as regions of least solar system and galactic foreground, not based upon the outcome of isotropy tests of residuals. Since the HQA region contains evident model artifacts, the remaining tests were restricted to the HQB region.

A more general test for structure within an area, such as the HQB region, is to fit a trend surface. If the scatter of the residuals of the fit is significantly less than the scatter about the mean value in the patch, structure exists. To determine the significance of a measure of scatter in a patch, without making any assumptions about the nature of the data, the intensity values of its pixels were randomly permuted spatially, creating a “flat” reference patch. Applying a surface fit to many such randomized versions of a patch allowed the derivation of the empirical distribution function of the χ^2 of the fit to a flat patch. The same type of surface was then fitted to the actual patch data (no permutation), and the χ^2 calculated. The fraction of randomized patches with smaller values of χ^2 is the significance level to which the patch is flat. This analysis was performed individually on the two HQB patches, using polynomials through degree n in a galactic coordinate system, l and $\csc b$.

Table 4 lists the results of this analysis applied to the separate north and south halves of the HQB region (HQBN and HQBS) for a surface of up to degree 3 (10 terms). The entries at wavelengths of 12 to 100 μm are omitted since at these wavelengths the residuals are clearly not isotropic: surface trends are obvious and the significance level of flatness less than 0.1%. The HQBS region at 4.9 μm also bears evidence of structure, but the test was inconclusive for the other entries in Table 4.

One can only say they are consistent with being flat. However, there may be clustering or some other irregular structure which, to a smooth polynomial surface, appears as noise.

3.5.4. Two-Point Correlation Functions

A more sophisticated test of the isotropy of the residual infrared emission is the two-point correlation function of the residuals. The procedures used were very similar to those employed for the analysis of the CMB anisotropy in the *COBE*/DMR data (Hinshaw et al. 1996). The two-point correlation function is expressed as $C(\theta) = \langle \nu I_i \nu I_j \rangle$ where the angle brackets denote the average over all N_{ij} pixel pairs in the region of interest that are separated by an angular distance θ . The pixel intensities, I_i , have had the mean residual intensity (i.e., the monopole term) subtracted.

Figures 3a, 3b, and 3c show the two-point correlation functions for the 3.5, 100, and 240 μm residual emission in the HQB region. The correlation function is binned into $0^\circ 25$ bins, which is slightly less than half of the width of the DIRBE beam. The degree of isotropy of the two-point correlation function was evaluated by comparing the correlation function of the real data with two-point correlation functions generated from an ensemble of Monte Carlo simulations of the residual brightness in the HQB regions. The simulations assumed zero mean intensities with random Gaussian uncertainties in each pixel that were estimated from the weekly variation of the observed data, after removal of the IPD emission (see Paper III for details). We increased the number of simulations until the statistical results (below) were unaffected by the size of the sample. This required 7200 simulations at 240 μm (9600 for ISM2), and 4800 simulations at 140 μm . At other wavelengths, comparison of the observed correlation function with the theoretical uncertainties ($\sigma_{C(\theta)} = \sigma_I^2 / \sqrt{N_{ij}}$, assuming that a single σ_I applies for all pixels) was sufficient to demonstrate a clear lack of isotropy.

For the data and each of the simulations, a χ^2 statistic

TABLE 4
TEST FOR SURFACE TRENDS IN HQB

Surface	Flatness of HQBN, HQBS (%)					
	1.25 μm	2.2 μm	3.5 μm	4.9 μm	140 μm	240 μm
$P_1(l, \csc b)$	47, 36	50, 43	48, 45	28, 10	50, 52	51, 52
$P_2(l, \csc b)$	46, 26	48, 29	38, 40	22, 6	50, 50	52, 49
$P_3(l, \csc b)$	44, 24	46, 39	38, 39	23, 4	50, 49	53, 50

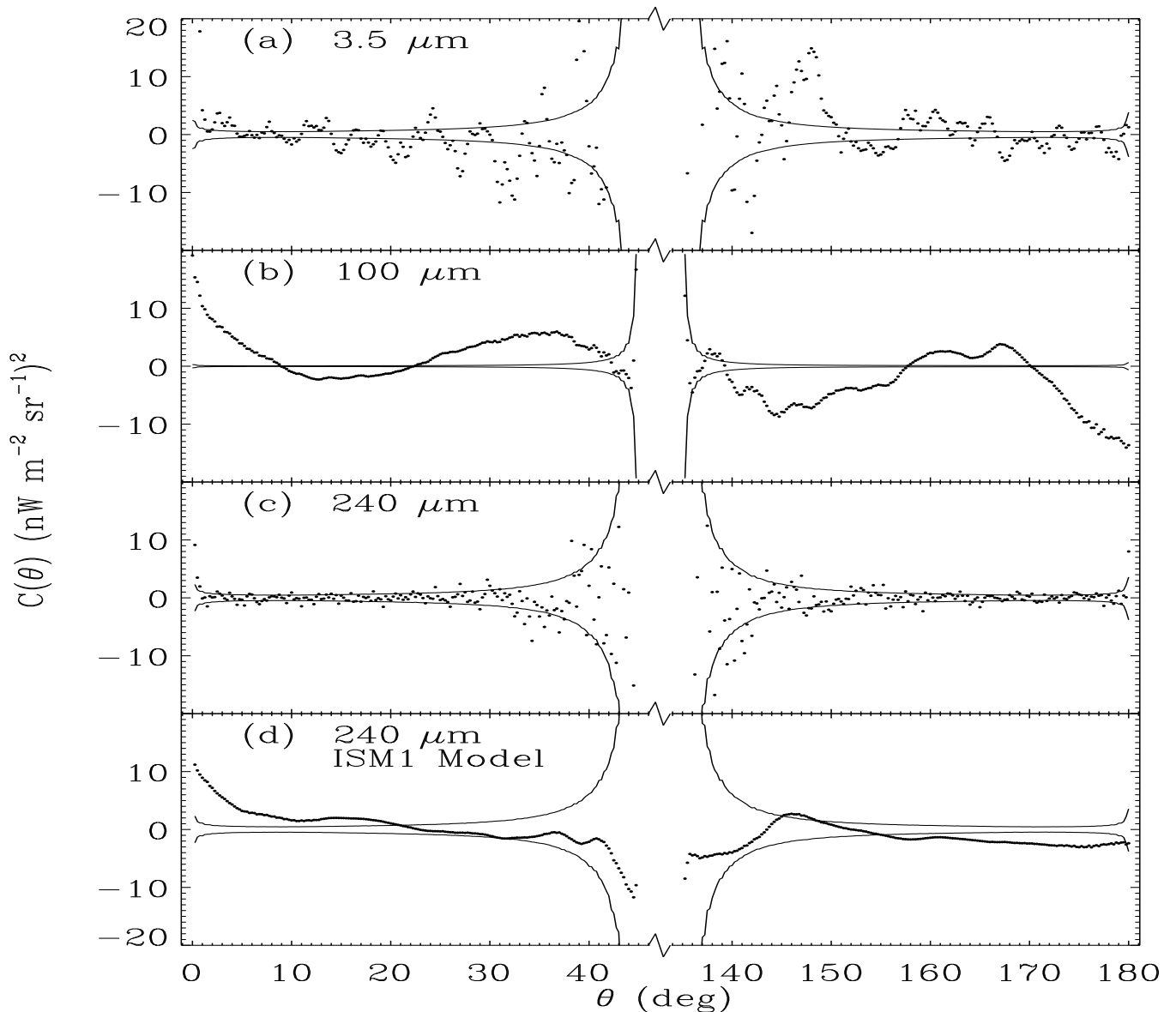


Fig. 3.—Two-point correlation function used to test the isotropy of the DIRBE residual emission in the high quality region B (Table 3). The top three panels show the correlation functions of the residuals at three wavelengths, while the bottom panel shows the correlation function of the interstellar medium model (ISM1) at $240\ \mu\text{m}$. The solid lines in each panel are the $\pm 1\sigma$ uncertainties estimated by Monte Carlo simulations. Separations of $0^\circ \leq \theta < 45^\circ$ are obtained within each of the north and south high quality B regions, while separations of $135^\circ < \theta \leq 180^\circ$ are obtained between the north and south high quality B regions. The large uncertainties at $\theta \approx 45^\circ$ and 135° are due to the small number of pixel pairs at these separations.

was calculated as

$$\chi^2 = \Delta\mathbf{C}^T \cdot \mathbf{M}^{-1} \cdot \Delta\mathbf{C} \quad (3)$$

where $(\Delta\mathbf{C})_i = C(\theta_i) - \sigma^2\delta(0)$ is the difference between the correlation function of the data (or one of the simulations) and the correlation function for a per-

fectly isotropic distribution [$C(\theta) = 0$ except $C(0) = \sigma^2$] and \mathbf{M}^{-1} is the inverse of the correlation matrix $\mathbf{M} = \langle (\Delta\mathbf{C})(\Delta\mathbf{C})^T \rangle$, where the angle brackets here denote an average over all Monte Carlo simulations. If there were no cross-correlation between the terms of the two-point correlation function, this definition of χ^2 would reduce to the usual form. The lines in the two-

point correlation of Figure 3c indicate the $\pm 1\sigma$ (rms) variations in $C(\theta)$ for all the simulated correlation functions at 240 μm . In Figures 3a and 3b, the lines indicate the theoretically expected variation of $\sigma^2/\sqrt{N_{ij}}$ for the 3.5 and 100 μm data.

Ideally, if the data are isotropic the reduced χ^2 , χ_ν^2 , should be ≈ 1.0 and the fraction of simulations that have a smaller χ^2 than the data should be $P(< \chi^2) \approx 0.5$. Table 5 lists the results at 240 μm for the entire HQB region, and for the north and south halves considered independently. The results of the analysis of the residuals from the two-component ISM model (ISM2) are also presented. Within the subsets of the HQBS (ISM1) and HQBN (ISM2) regions, the 240 μm data are found to be indistinguishable from the random simulations. In the full HQB region, the $P(< \chi^2)$ values, while more marginal, do not support rejection of the hypothesis that the residual 240 μm emission in the HQB region is isotropic. As a further comparison, Figure 3d shows the correlation function in the HQB region for the ISM1 model used in creating the 240 μm residual map. Structure of this character is absent in the 240 μm residual map (Fig. 3c). The 100 μm ISM map was clearly a good template for the 240 μm ISM emission. On the other hand, the large features in the correlation function of the 100 μm residual map (Fig. 3b), which was created using an H I map as the ISM template, indicate that there generally are some deficiencies in the assumption that H I is an accurate spatial tracer of dust (as noted in § 3.4).

For the 140 μm residual emission, the case for isotropy of the residual emission is not as strong, but is still not thoroughly rejected (Table 5). At wavelengths shorter than 140 μm , isotropy can be ruled out by the fact that the two-point correlation functions display significant structure (caused by imperfect removal of foreground emission) and $\chi_\nu^2 \gg 1.0$ (e.g., Figs. 3a and 3b).

As a further check on the isotropy of the residual emission in the HQB region, we also calculated the two-point cross-correlations between the residual 140 μm emission and the IPD and ISM models used in deriving those residuals. The same cross-correlations were calculated for both the ISM1 and ISM2 residual emission maps at 240 μm . Table 5 shows the results of these cross-correlations. The cross-correlations indicate isotropy at about the same level of confidence as the auto-correlations.

Table 5 also includes the results found when the two-point correlation functions of the residual emission at 140 and 240 μm are calculated over the region of the Lockman hole. For this test, the residual emission was generated by the subtraction of the H I emission scaled by the slope of the H I - IR correlation (§ 3.4), rather

than the standard 100 μm template of the ISM emission. The LH region is smaller than the HQB region, and only samples angular separations in the range $0^\circ \leq \theta \lesssim 22^\circ$. Using the H I column density as the ISM template, the 140 μm residual emission in the LH region exhibits isotropy at roughly the same level of confidence as does the 140 μm residual in the HQB region when the 100 μm data are used as the ISM template. At 240 μm , use of the H I data as the ISM template leads to residuals that are indistinguishable from the random simulations. Apparently, within this region of low H I column density, there is little or no indication of anisotropic emission from the ionized and molecular phases of the ISM.

Two-point correlation functions for the 140 and 240 μm residual emission often exhibit an increase at the smallest angular scales, $\theta < 1^\circ$ (e.g., Fig. 3c). However, any apparent correlation on these roughly beam-sized angular scales does not strongly influence the overall correlation statistics. When the statistics of the correlation functions are calculated excluding correlations on angular scales smaller than 1° , the values of χ_ν^2 show only modest decreases at best, and the corresponding probabilities for isotropy are only slightly improved. Examples of these are given in the last columns of Table 5.

Finally, to place limits on the *anisotropy* of the 240 μm residual emission within the HQB region, a technique commonly used to limit temperature fluctuations in the CMB is employed (e.g., Readhead et al. 1989; Church et al. 1997). The observed correlation function is compared with Gaussian autocorrelation function (GACF) models of the form $C(\theta) = C_0(\theta_c) \exp(-\theta^2/2\theta_c^2)$, where θ_c is the intrinsic correlation scale of the fluctuations and $C_0^{1/2}(\theta_c)$ is their mean amplitude. Convolution of intrinsic fluctuations with a Gaussian approximation to the DIRBE beam [$\exp(-\theta^2/2\theta_0^2)$ with $\theta_0 \approx 0.3^\circ$] gives a correlation function of the form:

$$C(\theta) = C_0(\theta_c) \frac{\theta_c^2}{2\theta_0^2 + \theta_c^2} \exp\left[-\frac{\theta^2}{2(2\theta_0^2 + \theta_c^2)}\right]. \quad (4)$$

Fitting this model to the data provides limits on $C_0(\theta_c)$. For the HQB region and the 240 μm residual emission after removal of the ISM1 model, the best fit GACF has an amplitude of $C_0(\theta_c) \frac{\theta_c^2}{2\theta_0^2 + \theta_c^2} = 10 \pm 2 \text{ nW m}^{-2} \text{ sr}^{-1}$ and an apparent scale length $2\theta_0^2 + \theta_c^2 \approx 2\theta_0^2$. If this correlation is removed, there is no other correlation on angular scales larger than $\sim 2^\circ$, limited by $C_0(\theta_c) < 1 \text{ nW m}^{-2} \text{ sr}^{-1}$. For the 240 μm residual emission after removal of the ISM2 model, correlation is again found on a scale comparable to the beam, but with an increased amplitude of $C_0(\theta_c) \frac{\theta_c^2}{2\theta_0^2 + \theta_c^2} = 50 \pm 20 \text{ nW m}^{-2} \text{ sr}^{-1}$. Fluctuations on other scales can not be limited as tightly as for the residual emission of the ISM1 model subtrac-

tion. The small-scale angular correlation appearing in the first several angular bins of the 240 μm plot has been investigated. Residual structures in the IPD cloud and interstellar medium do not produce effects this large. The extrapolated emission of the sources in the *IRAS* Point Source Catalog also does not produce this much correlated power. After the small-scale angular correlation was found in the residual maps, a weak time correlation in successive samples of the 240 μm dark noise data (DIRBE shutter closed) was found. This temporal correlation maps into adjacent pixels in the sky, and is large enough to produce the observed small-angle cor-

relation. However, the cause of this unexpected instrumental effect is not known.

3.6. Conclusions from Residuals

The signatures of a candidate CIB detection are a significantly positive residual and isotropy over the tested area of the sky. We require that a significant mean residual exceed 3σ , where the uncertainty, σ , is the quadrature sum of the random errors and systematic uncertainties of the measurements and foreground removal. The smallest sky area considered meaningful for isotropy testing is the 2% of the sky where there are generally

TABLE 5
RESULTS FROM TWO-POINT CORRELATION

Wavelength (μm)	Location	$0^\circ \leq \theta \leq 180^\circ$		$1^\circ \leq \theta \leq 180^\circ$	
		$\chi_\nu^2{}^a$	$P(< \chi_\nu^2)^b$	$\chi_\nu^2{}^a$	$P(< \chi_\nu^2)^b$
140	HQB	1.31	0.99	1.24	0.97
140	HQBN	1.24	0.92	1.16	0.85
140	HQBS	1.09	0.75	1.05	0.67
140 ^c	LH	1.27	0.91
240	HQB	1.19	0.95	1.13	0.87
240	HQBN	1.34	0.97	1.31	0.96
240	HQBS	1.06	0.68	0.98	0.48
240 ^c	LH	0.94	0.41
240 ^d	HQB	1.10	0.83	1.10	0.81
240 ^d	HQBN	0.99	0.52	1.00	0.54
240 ^d	HQBS	1.13	0.80	1.13	0.81
<hr/>					
140 \times IPD	HQB	1.21	1.00
140 \times IPD	HQBN	1.09	0.81
140 \times IPD	HQBS	1.30	1.00
140 \times ISM	HQB	1.28	1.00
140 \times ISM	HQBN	1.16	0.93
140 \times ISM	HQBS	1.15	0.92
240 \times IPD	HQB	1.12	0.95
240 \times IPD	HQBN	0.99	0.48
240 \times IPD	HQBS	1.17	0.95
240 \times ISM	HQB	1.13	0.95
240 \times ISM	HQBN	1.03	0.63
240 \times ISM	HQBS	1.07	0.77
240 ^d \times IPD	HQB	1.21	1.00
240 ^d \times IPD	HQBN	1.05	0.71
240 ^d \times IPD	HQBS	1.29	1.00
240 ^d \times ISM	HQB	1.16	0.98
240 ^d \times ISM	HQBN	1.06	0.71
240 ^d \times ISM	HQBS	1.06	0.73

^a For $0^\circ \leq \theta \leq 180^\circ$: $\nu = 360$ for HQB and $\nu = 180$ for HQBN and HQBS. For $1^\circ \leq \theta \leq 180^\circ$: $\nu = 356$ for HQB and $\nu = 176$ for HQBN and HQBS.

^b The probability of one Monte Carlo simulation having a smaller χ_ν^2 than the value listed in the preceding column.

^c Residuals after subtraction of the Snowden et al. (1994) H I data as the ISM model.

^d Residual at 240 μm after subtraction of the 2-component ISM model (ISM2).

minimal foregrounds, the HQB region.

Within the HQB region, there are gradients in the residual emission and little or no consistency with isotropy in the two-point correlation functions and other isotropy tests for all wavelengths from 1.25 to 100 μm . Furthermore, at all of these wavelengths, with the exception of 4.9 μm , the mean residual emission is less than 3σ . Therefore, from 1.25 to 100 μm , we are only able to establish upper limits on an isotropic background. Using the HQB analysis, upper limits at the 95% confidence level (CL) are taken to be the residual intensities, $\nu I_0(\text{HQB})$, plus twice the quadrature sum of their random and systematic uncertainties. These upper limits are listed as νI_0 (95% CL) in Row 17 of Table 2.

At 140 and 240 μm the two-point correlation functions indicate that the residual emission is isotropic over the HQB region, particularly if the North and South halves of the region are considered separately (Table 5). The absence of significant gradients with ecliptic or galactic latitude (Table 2, rows 15–16) also supports this conclusion. However, the mean residuals at these wavelengths in the HQB region alone does not exceed 3σ , primarily as a result of the large systematic uncertainty arising from using the 100 μm map as the ISM template. As discussed in § 3.4, direct correlation of the infrared emission with the H I column density in the well-studied LH' region at the Lockman hole results in smaller systematic uncertainties in the residual intensities than yielded by our map-based procedures for subtracting the ISM contribution in HQB. The same is true at 240 μm for the NEP' region at the north ecliptic pole. In particular, the correlation procedure yields residual intensities in the Lockman hole region that are greater than 3σ at 100, 140 and 240 μm , and that are consistent with the mean residuals and their uncertainties in the HQB and NEP' regions.

In order to make full use of the most accurate determinations of the residuals at these long wavelengths, the weighted average of the residuals in the HQB, LH'(HI) and NEP'(HI) regions was determined. The weighting factors are the inverse squares of the combined random and non-common-mode systematic uncertainties for the three regions. For these purposes, gain, offset, and IPD model errors were considered common-mode errors, leaving the uncertainty in the ISM removal as the systematic error. This weights the LH'(HI) determination most heavily. Row 18 of Table 2 shows the resulting weighted averages, $\langle \nu I_0 \rangle$, at 100, 140, and 240 μm . The uncertainties in these values include the formal propagated uncertainty of the averaging process added in quadrature with the common-mode systematic uncertainties excluded in the averaging.

Since the weighted-average residuals at 140 and 240

μm , $\nu I_\nu = 25 \pm 7$ and 14 ± 3 $\text{nW m}^{-2} \text{sr}^{-1}$ respectively, exceed 3σ and satisfy the isotropy tests, these residuals are either detections of the CIB or unmodeled isotropic contributions from sources in the solar system or Galaxy. Arguments against the foreground interpretation are presented in Paper IV and summarized in § 4.1. Though the weighted-average residual at 100 μm in the HQB region, Lockman hole, and north ecliptic pole regions exceeds 3σ , the anisotropy in the HQB region excludes this as a candidate detection of the CIB. The anisotropy at 100 μm may be the result of inaccuracy in the ISM model due to use of the H I template (§ 3.4), as well as the appreciable artifacts from the IPD model at this wavelength. The weighted-average residual at 100 μm provides a slightly more restrictive upper limit on the CIB than the HQB analysis alone. The last row of Table 2 shows the values of the two measurements of the CIB at 140 and 240 μm and the most restrictive upper limits at all other wavelengths.

4. DISCUSSION AND CONCLUSIONS

4.1. Possible Contributions from Unmodeled Isotropic Sources

In order to verify that the probable isotropic residual emission at 140 and 240 μm is of extragalactic origin, we need to demonstrate that local contributions of isotropic or nearly isotropic components, both within the solar system and within the Galaxy, do not contribute significantly to the residual emission. Circumterrestrial material is ruled out by lack of variation of the measured sky brightness with zenith angle, and by the low color temperature of the residual radiation. Heliocentric material within the solar system may have escaped our modeling efforts if it lies in the outer solar system, where its intensity will show little or no modulation as the Earth moves along its orbit. Such a cloud would not have been detectable by the IPD modeling procedures applied, which relied on the apparent temporal variations of the IPD emission. An isotropic component of the Galactic emission may not have been removed by our models if it arises from sources distributed in a roughly spherical halo around the Galactic center of radius much larger than 8.5 kpc.

These potential solar system and Galactic sources are considered in detail in Paper IV. In the case of the solar system, it is shown that a spherical cloud formed early in the history of the solar system would not survive to the present. A persistent spherical cloud would require a source of replenishment, and no plausible source for a cloud of adequate mass can be identified. Difficulties with attributing a significant portion of the 140 and 240

μm isotropic residual emission to a Galactic dust component include the lack of a plausible mechanism for creating and maintaining a large, smooth, shell-like distribution of dust, and the absence of a heating source which could maintain a uniform dust temperature as high as that implied by the detections (~ 17 K) at large distances from the Galactic plane. Furthermore, such a shell would require such a large dust mass that the associated gas mass would be at least comparable to that in the Galactic disk (assuming metallicity no greater than solar).

Hence, there is no known or likely source, consistent with other present knowledge of the solar system and Galaxy, which can meet the combination of constraints imposed by the low color temperature and isotropy of the long wavelength residual detections. We conclude that it is unlikely that significant fractions of the observed 140 and 240 μm residual emission can arise from either an IPD or a Galactic emission component. The most likely conclusion is that these signals arise from an extragalactic infrared background.

4.2 Comparison with Previous Limits

4.2.1. Direct Infrared Brightness Measurements

Figure 4 summarizes the current state of direct infrared background measurements. DIRBE results presented in this paper are shown from 1.25 to 240 μm for both the dark sky upper limits (2σ above the lowest measured values, from Table 2) and the limits and detections after foreground removal. Dark sky upper limits from 120 to 650 μm determined in “broad bands” from *COBE*/FIRAS data (Shafer et al. 1998) are also shown. In the 140–240 μm region, the FIRAS dark sky limits are in excellent agreement with the corresponding DIRBE limits. Since the calibrations of the two instruments are very consistent (Fixsen et al. 1997), this suggests that there are no small regions (on the scale of the DIRBE beam) in which the DIRBE has a better view beyond the Galaxy than does the FIRAS with its much larger beam.

Near-infrared limits from recent rocket measurements (Matsuura et al. 1994) are similar to the DIRBE dark sky limits, whereas the “unknown residual emission” after foreground removal by Noda et al. (1992) is close to the foreground-removed DIRBE upper limits. For comparison, an upper limit obtained from sky photometry in the optical is also shown (Mattila 1990). Far-infrared limits from the rocket data of Kawada et al. (1994) are generally similar to the *COBE* dark sky values, though the quoted residual upper limit at 154 μm is very close to the DIRBE detection at 140 μm . Schlegel, Finkbeiner, & Davis (1997) have recently studied Galactic reddening

using DIRBE long wavelength data as a tracer of the interstellar dust. Using a simpler long-wavelength IPD model than ours (Paper II), they have found uniform backgrounds at 140 and 240 μm which they identify as CIB detections at levels similar to the residual values reported here.

Figure 4 also shows the tentative detection of a 170 – 1260 μm background based upon FIRAS data reported by Puget et al. (1996). This result is significantly below the 140 – 240 μm detections reported here. Even if the DIRBE result were to be recalibrated using the DIRBE–FIRAS calibration comparison of Fixsen et al. (1997), this significant difference would remain. We have no ready explanation for that difference. However, Fixsen et al. (1998) have recently completed an extensive assessment of the evidence for the CIB in the FIRAS data. In order to investigate the magnitude of the systematic uncertainties involved in separating Galactic emission from the CIB, they have used three independent methods to derive the CIB spectrum. One of these methods assumes that our DIRBE results are correct, and so we ignore that one here for purposes of comparing the DIRBE and FIRAS results. Figure 4 shows the average of the Fixsen et al. (1998) results using two other methods for separation of Galactic emission: a method based upon assuming a single color temperature for the ISM emission; and a method using maps of H I and C II emission to trace the ISM. Convolving this average of the results of Fixsen et al. (1998) with the DIRBE spectral responses at 140 and 240 μm yields FIRAS values at the same effective wavelengths of $\nu I_\nu = 11.5$ and $11.3 \text{ nW m}^{-2} \text{ sr}^{-1}$ respectively. These values are within 2σ and 1σ of the DIRBE results (Table 2) respectively, and so are entirely consistent with them. If we formally transform the DIRBE results to the FIRAS photometric scale according to the determination of Fixsen et al. (1997), we obtain $\nu I_\nu = 15.0$ and $12.7 \text{ nW m}^{-2} \text{ sr}^{-1}$ at 140 and 240 μm respectively. Thus, even the small difference between the DIRBE 240 μm result and that of Fixsen et al. (1998) arises in large part from the small difference in photometric scales of the two instruments, and not in the separation of the foreground radiations from the CIB. The difference between the experiments at 140 μm mostly arises from the calibration difference. We conclude that the FIRAS analysis of Fixsen et al. (1998) provides strong independent confirmation of the DIRBE observational conclusions.

4.2.2. Angular Fluctuation Limits

An alternative approach to searching for evidence of the CIB is to study the fluctuations in maps of the infrared sky brightness. If the spatial correlation function of the sources is known, the diffuse background

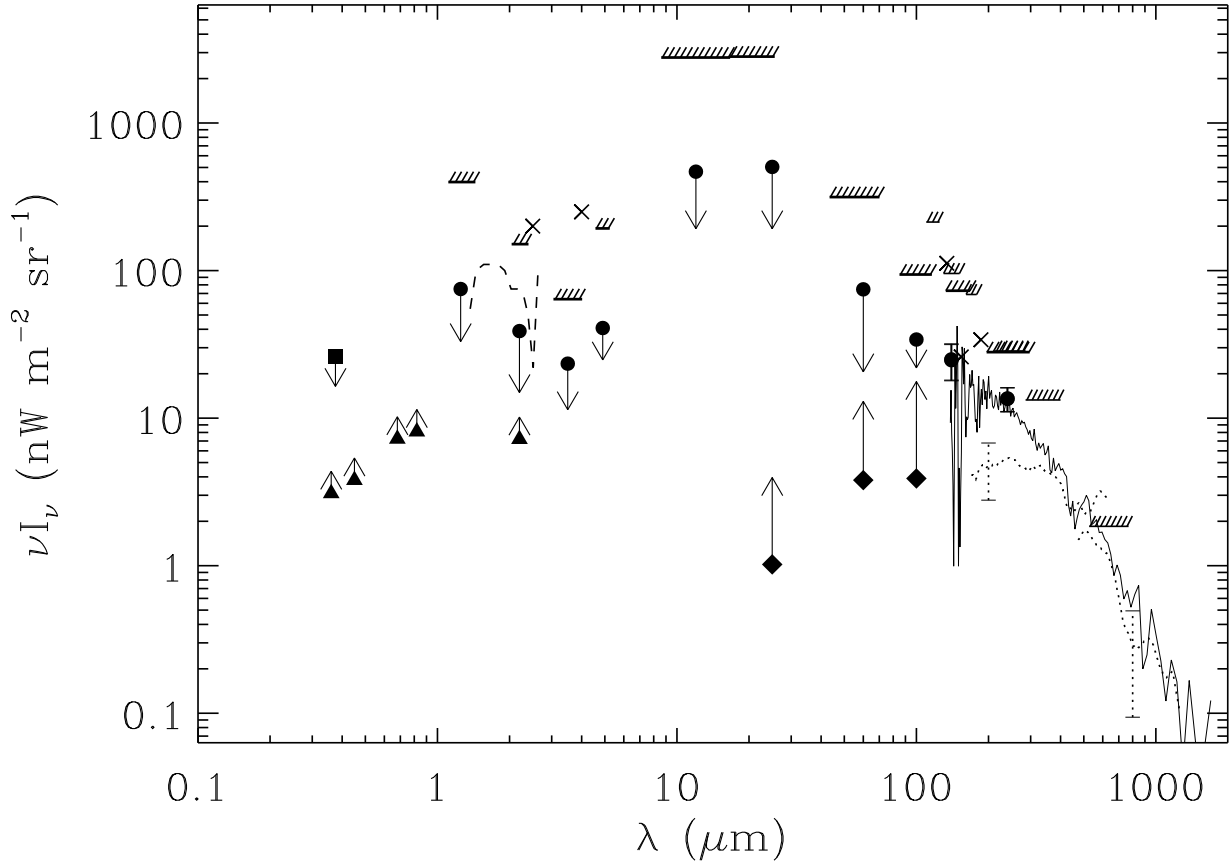


Fig. 4.—Cosmic background intensity I_ν times frequency ν as a function of wavelength λ . The circles with error bars are the detections based on DIRBE data after removal of foreground emission at 140 and 240 μm , while those with arrows are 2σ upper limits with the arrows extending to the measured residuals at 1.25 – 100 μm . The hatched thick lines are dark sky limits (95% CL) from the DIRBE data at 1.25 – 240 μm , while the hatched thin lines are dark sky “broad-band” limits (95% CL) from FIRAS data at 120 – 650 μm (Shafer et al. 1998). The crosses are upper limits derived from rocket experiments at 134 – 186 μm (Kawada et al. 1994) and 2.5 – 4.0 μm (Matsuura et al. 1994). The dashed line from 1.4 – 2.6 μm is residual radiation after foreground removal from the rocket data of Noda et al. (1992). The diamonds with arrows are lower limits derived from *IRAS* counts at 25 – 100 μm (Hacking & Soifer 1991; 60 μm limit from Gregorich et al. 1995). The dotted curve from 170 – 1260 μm shows the tentative infrared background determined from FIRAS data by Puget et al. (1996), while the solid curve is the average of the two DIRBE-independent methods of FIRAS analysis used by Fixsen et al. (1998). The triangles are lower limits derived from the Hubble Deep Field at 3600 – 8100 \AA (Pozzetti et al. 1998) and *K*-band galaxy counts at 2.2 μm (Cowie et al. 1994). The square is an upper limit derived from sky photometry at 4400 \AA (Mattila 1990).

produced by them can be estimated from the measured correlation function of sky brightness. Using such arguments, Kashlinsky et al. (1996a) obtained upper limits on the CIB from clustered matter of 200, 78, and 26 $\text{nW m}^{-2} \text{sr}^{-1}$ at 1.25, 2.2, and 3.5 μm respectively, values modestly above the present direct DIRBE brightness limits in Table 2 and Figure 4. In an extension of this approach, Kashlinsky et al. (1996b) deter-

mined the rms fluctuations in the DIRBE maps from 2.2 – 100 μm , and argue that these values imply that the CIB due to matter clustered like galaxies is less than about 10 – 15 $\text{nW m}^{-2} \text{sr}^{-1}$ over this wavelength range. In the near infrared and at 100 μm , these values are close to the observed residuals reported in Table 2. In the thermal infrared region, 12 – 60 μm , where the accurate removal of the large contribution from the in-

terplanetary dust is so difficult, these limits are much below the limits reported here. However, relating the limit on rms map fluctuations to the absolute brightness of the sky does involve model-dependent assumptions about the clustered sources of radiation.

4.2.3. Limits from TeV Gamma Rays

Indirect evidence for the CIB can be obtained in principle by observing attenuation of very energetic γ -rays from extragalactic sources (Gould & Schreder 1967). Attenuation will arise from pair-production in the interaction of the γ -rays with infrared photons. Such arguments, based upon apparent evidence for attenuation of TeV γ -rays from Mk 421, have been used to obtain both upper and lower limits on the CIB. The limits obtained depend on the assumed spectrum of the CIB, as well as of the intrinsic spectrum of the γ -ray source (de Jager, Stecker, & Salamon 1994; Dwek & Slavin 1994; Biller et al. 1995; Stecker 1996; Stecker & de Jager 1997). However, Krennrich et al. (1997) have recently reported detection of γ -rays with energies exceeding 5 TeV from Mk 421. These authors conclude that there is no present evidence in the data for attenuation by pair production on optical or near-infrared photons, though given the uncertainty in the intrinsic γ -ray source spectrum, the possibility of some such attenuation can not be totally ruled out. Under the above assumptions, even with no evident attenuation, these observations provide upper limits on the CIB between 15 and 40 μm of about 10 – 20 $\text{nW m}^{-2} \text{sr}^{-1}$ (e.g., Dwek & Slavin 1994). These limits are well below the present direct limits from DIRBE data, and are comparable to those obtained by Kashlinsky, Mather & Odenwald (1996b) from their analysis of fluctuations in the DIRBE maps (§ 4.2.2). Recent analysis of the TeV γ -ray data from Mk 501 by Stanev and Franceschini (1997) yields limits from 1 to 40 μm in the range 1 – 20 $\text{nW m}^{-2} \text{sr}^{-1}$ depending upon the assumed spectrum of the CIB. Because of the large observational and theoretical uncertainties inherent in these limits, we do not yet regard them as strong constraints on currently popular theoretical models of the CIB in this wavelength interval (Paper IV).

4.3. Relationship to Integrated Brightness of Galaxies

Lower limits to the extragalactic infrared background can be obtained by integrating the brightness of observed galaxies. Figure 4 shows such results from the near-infrared galaxy counts of Cowie et al. (1994), and from the *IRAS* survey by Hacking & Soifer (1991) and Gregorich et al. (1995). The *IRAS* results are shown as a range to encompass the various galaxy luminosity or density evolution models considered. Figure 4 also shows lower limits at UV and optical wavelengths

derived from galaxy counts in the Hubble Deep Field (Pozzetti et al. 1998). It is comforting to see that the integrated discrete source estimates still lie below the diffuse sky brightness residuals, and the gap is not large at some wavelengths. For example, the bright end of the evolution models considered by Hacking & Soifer (1991) at 60 and 100 μm [as amended by Gregorich et al. (1995) at 60 μm] is only about a factor of two below the DIRBE measured residuals at the corresponding wavelengths. The estimated integrated galaxy far-infrared background contribution should become less uncertain as deeper counts from space missions such as *ISO*, *WIRE*, and *SIRTF* are obtained.

4.4. Limit on Integrated Infrared Background

The CIB limits and detections reported here provide an upper limit on the integrated energy density of the CIB, an overall constraint on the integrated cosmic luminosity. Denoting the integrated infrared background energy density in units of the critical closure energy density by Ω_{IR} and the corresponding quantity for the CMB by Ω_{CMB} , one finds that (for $T_{CMB} = 2.728 \text{ K}$, Fixsen et al. 1996) $\Omega_{IR}/\Omega_{CMB} = 1 \times 10^{-3} \times (I_{IR}/\text{nW m}^{-2} \text{sr}^{-1})$, where I_{IR} is the sky brightness integrated over the infrared spectrum. Taking the range of integration for the infrared to be 1 – 300 μm , the dark sky upper limits of Table 2 give $\Omega_{IR}/\Omega_{CMB} < 2.4$, not a very restrictive limit. If the DIRBE upper limits plus likely detections shown in Table 2 are used, one finds an upper limit of $\Omega_{IR}/\Omega_{CMB} < 0.5$.

To provide substantially more stringent limits on the integrated infrared background over this broad spectral range, the peak in the limits over the thermal infrared range ($\sim 5 - 60 \mu\text{m}$), which may largely be due to the difficulty in discriminating the IPD signal to better than a few percent of its value, must be substantially reduced. However, the limits on both the short-wavelength and long-wavelength sides of this peak are themselves of interest, since they constrain both the directly radiated energy density and that due to primary radiation absorbed by dust and re-emitted at longer wavelengths. The strong upper limits found from the dark sky upper limits of Table 2 are $\Omega_{IR}/\Omega_{CMB} < 0.16$ and $\Omega_{IR}/\Omega_{CMB} < 0.05$ in the ranges 1 – 5 μm and 100 – 240 μm respectively. Using the foreground-removed upper limits and detections from Table 2, the corresponding limits are $\Omega_{IR}/\Omega_{CMB} < 0.04$ and $\Omega_{IR}/\Omega_{CMB} < 0.02$.

4.5. Implications

The DIRBE CIB detections and upper limits cover a broad spectral range from 1.25 μm to 240 μm . The CIB intensity in the 1.25 – 5 μm range is likely dominated by direct starlight from galaxies, whereas the intensity in

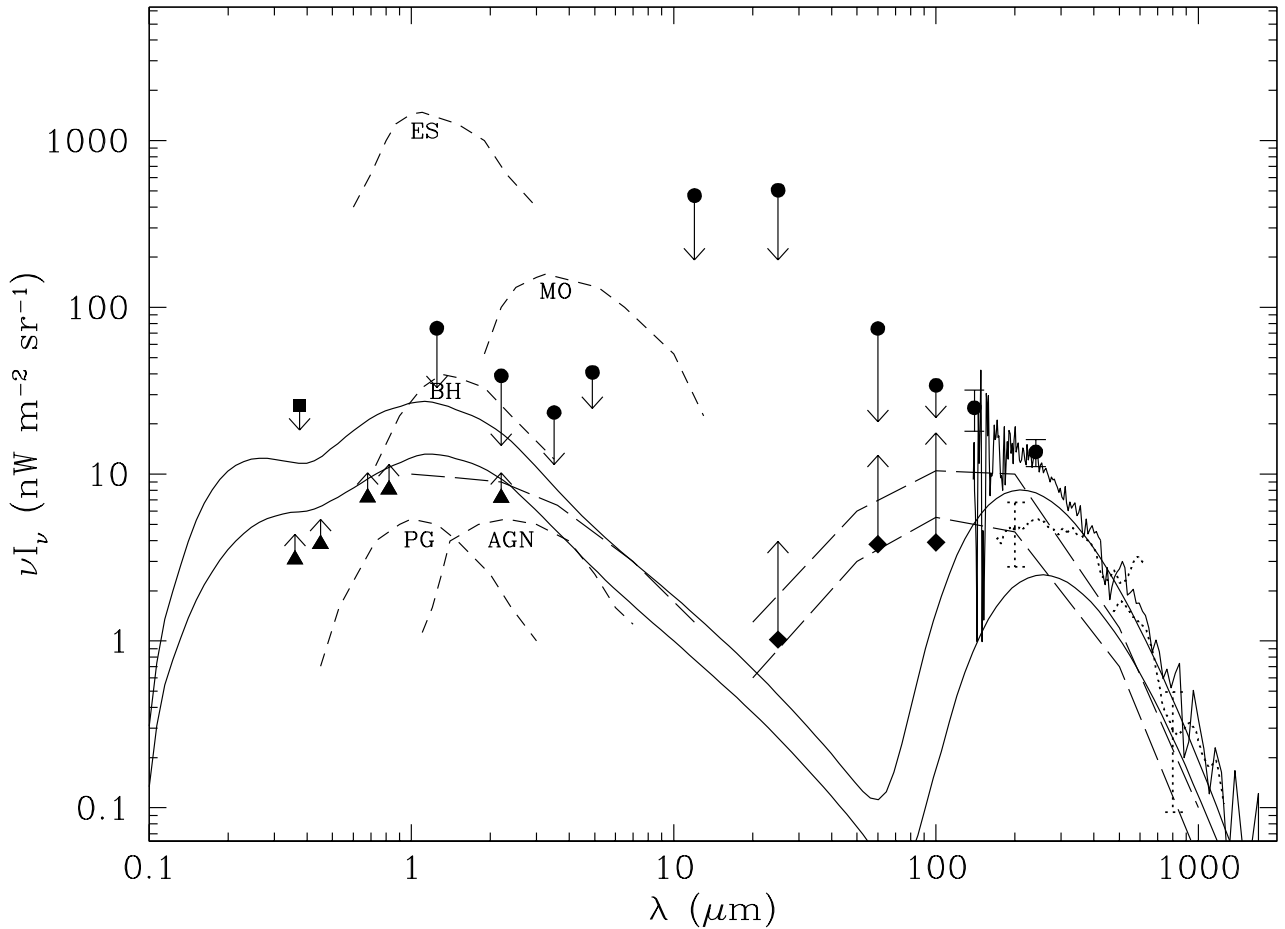


Fig. 5.—Predicted contributions to the cosmic infrared background radiation. The data points and FIRAS curves are the same measurement results as in Fig. 4. The short-dashed lines show CIB estimates by Bond, Carr, & Hogan (1991) for some possible pregalactic and protogalactic sources in a dust-free universe, including exploding stars (ES), massive objects (MO), halo black holes (BH), active galactic nuclei (AGN), and primeval galaxies (PG). The long-dashed lines are calculations of Franceschini et al. (1994) using models of photometric evolution of galaxies with two cases of dust opacity. The solid lines are calculations of Fall, Charlot, & Pei (1996) using closed-box (lower curve) and inflow (upper curve) models of cosmic chemical evolution.

the 100–240 μm range is likely dominated by reradiated starlight from dust within galaxies. Under these assumptions, one of the important implications of the DIRBE results is that they provide valuable constraints on the global history of star formation and dust production in the universe. In general, the CIB is a fossil containing the cumulative energy release of astrophysical objects or processes in the universe. The DIRBE results can therefore be used to discriminate and constrain possible contributors to the CIB, such as active galactic nuclei, halo black holes, pregalactic stars, decaying particles, and gravitational collapse (e.g., Bond, Carr, & Hogan 1991). Here we briefly discuss the implications of our

measurements for star formation and dust production in galaxies based largely upon published models. Paper IV provides more extensive discussion of the cosmological implications.

One of the surprising consequences of the DIRBE results presented here is that the detected energy level of the far-IR background, $\int \nu I_\nu d \ln \nu = 10.3 \text{ nW m}^{-2} \text{ sr}^{-1}$ in the 140–240 μm range, is a factor of ~ 2.5 higher than the integrated optical light from the galaxies in the Hubble Deep Field, $\int \nu I_\nu d \ln \nu = 4.2 \text{ nW m}^{-2} \text{ sr}^{-1}$ in the 3600–8100 \AA range (Pozzetti et al. 1998). Since the full spectrum of the cosmic background in the UV-optical and far-infrared wavelength ranges is unknown,

the exact ratio of the backgrounds in these ranges is still quite uncertain. Nevertheless, the DIRBE detections, when compared with the Hubble Deep Field results, indicate that a substantial fraction of the total stellar luminosity from galaxies might have been reradiated by dust in the far-infrared at the expense of the obscured UV-optical luminosity. This implies that star formation might be heavily shrouded by dust at high redshifts.

Figure 5 shows the same data as in Figure 4, superimposed on CIB estimates for some early models of possible pregalactic and protogalactic sources in a dust-free universe (Bond, Carr, & Hogan 1991). Clearly the DIRBE upper limits in the near-infrared and the lower limits from deep optical and near-infrared galaxy counts either rule out such models or require revision of their parameters. Figure 5 also shows two examples of the predicted contributions of galaxies to the CIB. The dashed curves are the calculations of Franceschini et al. (1994) using evolutionary models with moderate and opaque dust optical depth, largely based on emission properties of galaxies at the present epoch. The solid curves are the calculations of Fall, Charlot, & Pei (1996) using closed-box and inflow models of cosmic chemical evolution, largely based on absorption properties of galaxies at different redshifts. Both classes of models modestly underpredict the DIRBE measurements of the far-infrared background. Since star formation and dust production are coupled, fitting CIB estimates from models of cosmic chemical evolution to the DIRBE detections can determine the rates of both star formation and dust production as a function of redshift. In this fashion, the DIRBE results taken together with deep optical surveys of galaxies promise to yield improved estimates of the history of global star formation, metal and dust production, and the efficiency of UV-optical absorption by dust.

4.6. Summary

The DIRBE investigation was designed to detect directly the CIB, or set limits on it imposed by the brightness of our local cosmic environment. The observational results reported here, supported by Papers II and III, show evidence for detection of such a background at the level of $25 \pm 7 \text{ nW m}^{-2} \text{ sr}^{-1}$ at $140 \mu\text{m}$ and $14 \pm 3 \text{ nW m}^{-2} \text{ sr}^{-1}$ at $240 \mu\text{m}$, and upper limits at wavelengths from 1.25 to $100 \mu\text{m}$. As our analyses show, the uncertainties in these results are indeed dominated by the uncertainties in our ability to discriminate or model the contributions to the infrared sky brightness from sources within the solar system and Milky Way Galaxy.

These results very substantially advance our prior direct knowledge of the extragalactic infrared sky bright-

ness, especially of what was known prior to the *COBE* mission. The quality of the DIRBE measurements themselves is such that improved knowledge of the local foregrounds could permit the search for the CIB to be carried to more sensitive levels using DIRBE data. Such knowledge will be provided by future measurements, such as the sensitive all-sky surveys at 2 microns (2MASS and DENIS) and more extensive measurements of Galactic H II emission at high latitudes, and possibly by improved techniques to model or discriminate the very dominant contribution from interplanetary dust (e.g., Gor'kavyi et al. 1997a; 1997b). Of course, further direct measurements of the absolute infrared sky brightness with higher angular resolution, preferably from a location more distant from the Sun so as to reduce the contribution of the interplanetary dust to the sky brightness, could advance this search dramatically.

The authors gratefully acknowledge the contributions over many years of the talented and dedicated engineers, managers, scientists, analysts, and programmers engaged in the DIRBE investigation. We thank G. Hinshaw for expert advice on two-point correlation functions. The National Aeronautics and Space Administration/Goddard Space Flight Center (NASA/GSFC) was responsible for the design, development, and operation of the *COBE*. Scientific guidance was provided by the *COBE* Science Working Group. GSFC was also responsible for the development of the analysis software and for the production of the mission data sets.

REFERENCES

- Arendt, R. G., Odegard, N., Weiland, J. L., Sodroski, T. J., Hauser, M. G., Dwek, E., Kelsall, T., Moseley, S. H., Silverberg, R. F., Leisawitz, D., Mitchell, K., & Reach, W. T. 1998, *ApJ*, submitted (Paper III)
- Biller, S. D., et al. 1995, *ApJ*, 445, 227
- Boggess, N. et al. 1992, *ApJ*, 397, 420
- Bond, J. R., Carr, B. J., & Hogan, C. J. 1986, *ApJ*, 306, 428
- Bond, J. R., Carr, B. J., & Hogan, C. J. 1991, *ApJ*, 367, 420
- Cohen, M. 1993, *AJ*, 105, 1860
- Cohen, M. 1994, *AJ*, 107, 582
- Cohen, M. 1995, *ApJ*, 444, 875
- Church, S. E., Ganga, K. M., Ade, P. A. R., Holzapfel, W. L., Mauskopf, P. D., Wilbanks, T. M., & Lange, A. E. 1997, *ApJ*, 484, 523

- COBE Diffuse Infrared Background Experiment (DIRBE) Explanatory Supplement, version 2.1, ed. M. G. Hauser, T. Kelsall, D. Leisawitz, and J. Weiland, COBE Ref. Pub. No. 97-A (Greenbelt, MD: NASA/GSFC), available in electronic form from the NSSDC at http://www.gsfc.nasa.gov/astro/cobe/cobe_home.html
- Cowie, L. L., Gardner, J. P., Hu, E. M., Songaila, A., Hodapp, K.-W., & Wainscoat, R. J. 1994, *ApJ*, 434, 114
- de Jager, O. C., Stecker, F. W. & Salamon, M. H. 1994, *Nature*, 369, 294
- Dwek, E. & Slavin, J. 1994, *ApJ*, 436, 696
- Dwek, E., Arendt, R. G., Hauser, M. G., Fixsen, D., Leisawitz, D., Pei, Y.C., Wright, E. L., Kelsall, T., Mather, J. C., Moseley, S. H., Odegard, N., Shafer, R., Silverberg, R. F., & Weiland, J. L. 1998, *ApJ*, submitted (Paper IV)
- Elvis, M., Lockman, F.J., & Fassnacht, C. 1994, *ApJS*, 95, 413.
- Evans, D. C. 1983, *Proc. SPIE*, 384, 82
- Fall, S.M., Charlot, S., & Pei, Y.C. 1996, *ApJ*, 464, L43
- Fixsen, D. J., Cheng, E. S., Gales, J. M., Mather, J. C., Shafer, R. A., & Wright, E. L. 1996, *ApJ*, 473, 576
- Fixsen, D. J., Weiland, J. L., Brodd, S., Hauser, M. G., Kelsall, T., Leisawitz, D. T., Mather, J. C., Jensen, K. A., Shafer, R. A., & Silverberg, R. F. 1997, *ApJ*, 490, 482
- Fixsen, D. J. et al. 1998, in preparation
- Franceschini, A., Toffolatti, L., Mazzei, P., & de Zotti, G. 1991, *A&AS*, 89, 285
- Franceschini, A., Mazzei, P., de Zotti, G., & Danese, L. 1994, *ApJ*, 427, 140
- Gor'kavyi, N. N., Ozernoy, L. M., & Mather, J. C. 1997a, *ApJ*, 474, 496
- Gor'kavyi, N. N., Ozernoy, L. M., Mather, J. C., & Taidakova, T. 1997b, *ApJ*, 488, 268
- Gould, R. J. & Schreder, G. 1967, *Phys. Rev.*, 155, 1408
- Gregorich, D. T., Neugebauer, G., Soifer, B. T., Gunn, J. E., & Herter, T. L. 1995, *AJ*, 110, 259
- Hacking, P. B., & Soifer, B. T. 1991, *ApJ*, 367, L49
- Hartmann, D., & Burton, W. B. 1997, *Atlas of Galactic Neutral Hydrogen*, (New York: Cambridge University Press)
- Harwit, M. 1970, *Rivista del Nuovo Cimento*, II, 253
- Hauser, M. G. 1995, in *Extragalactic Background Radiation*, Space Telescope Sci. Inst. Symp. Ser. 7, ed. D. Calzetti, M. Livio, & P. Madau, (Cambridge: Cambridge Univ. Press), 135
- Hauser, M. G. 1996a, in *Proc. IAU Symposium 168, Examining the Big Bang and Diffuse Background Radiations*, ed. M. Kafatos & Y. Kondo, (Dordrecht: Kluwer), 99
- Hauser, M. G. 1996b, in *Unveiling the Cosmic Infrared Background*, ed. E. Dwek (New York: IAP Press), 11
- Hinshaw, G., Banday, A. J., Bennett, C. L., Górski, K. M., Kogut, A., Lineweaver, C. H., Smoot, G. F., & Wright, E.L., 1996, *ApJ*, 464, L25
- Jahoda, K., Lockman, F. J., & McCammon, D. 1990, *ApJ*, 354, 184
- Kashlinsky, A., Mather, J. C., Odenwald, S., & Hauser, M. G. 1996a, *ApJ*, 470, 681
- Kashlinsky, A., Mather, J. C., & Odenwald, S. 1996b, *ApJ*, 473, L9
- Kawada, M., Bock, J. J., Christov, V. V., Lange, A. E., Matsuhara, H., Matsumoto, T., Matsuura, S., Mauskopf, P. D., Richards, P. L., & Tanaka, T. 1994, *ApJ*, 425, L89
- Kelsall, T., Weiland, J. L., Franz, B. A., Reach, W. T., Arendt, R. G., Dwek, E., Freudenreich, H. T., Hauser, M. G., Moseley, S. H., Odegard, N. P., & Silverberg, R. F. 1998, *ApJ*, submitted (Paper II)
- Krennrich, F. et al. 1997, *ApJ*, 481, 758
- Lei96 Leinert, C. 1996, in *Unveiling the Cosmic Infrared Background*, ed. E. Dwek, (Woodbury, NY: AIP), 53
- Lockman, F. J., Jahoda, K., & McCammon, D. 1986, *ApJ*, 302, 432
- Magner, T. J. 1987, *OptEng*, 26, 264
- Matsumoto, T. 1990, in *The Galactic and Extragalactic Background Radiation*, IAU Symposium 139, ed. S. Bowyer & C. Leinert (Dordrecht: Kluwer), 317
- Matsumoto, T., Akiba, M., & Murakami, H. 1988, *ApJ*, 332, 575
- Matsuura, S., Kawada, M., Matsuhara, T., Noda, M., & Tanaka, M. 1994, *PASP*, 106, 770
- Mattila, K. 1990, in *IAU Symposium 139, The Galactic and Extragalactic Background Radiation*, ed. S. Bowyer & C. Leinert (Dordrecht: Kluwer), 257
- Noda, M., Christov, V. V., Matsuhara, H., Matsumoto, T., Matsuura, S., Noguchi, K., & Sato, S. 1992, *ApJ*, 391, 456
- Partridge, R. B. & Peebles, P. J. E. 1967, *ApJ*, 148, 377
- Pozzetti, L., Madau, P., Zamorani, G., Ferguson, H. C., & Bruzual, G. A. 1998, *MNRAS*, submitted
- Puget, J.-L., Abergel, A., Bernard, J.-P., Boulanger, F., Burton, W. B., Désert, F.-X., & Hartmann, D. 1996, *A&A*, 308, L5
- Readhead, A. C. S., Lawrence, C. R., Myers, S. T., Sargent, W. L. W., Hardebeck, H. E., & Moffet, A. T. 1989, *ApJ*, 346, 566
- Ressell, M. T. & Turner, M. S. 1990, *Comments on Astrophysics*, 14, 323
- Schlegel, D. J., Finkbeiner, D. P., & Davis, M. 1997, preprint
- Shafer, R. A., Mather, J. C., Fixsen, D. J., Jensen, K. A.,

- Reach, W. T., Wright, E. L., Dwek, E., & Cheng, E. S. 1998, preprint
- Silverberg, R. F. et al. 1993, Proc. SPIE Conf. 2019, Infrared Spaceborne Remote Sensing, ed. M. S. Scholl (Bellingham: SPIE), 180
- Snowden, S.L., Hasinger, G., Jahoda, K., Lockman, F.J., McCammon, D., & Sanders, W.T. 1994, ApJ, 430, 601
- Stanev, T. & Franceschini, A. 1997, ApJ, submitted
- Stark, A. A., Gammie, C. F., Wilson, R. W., Bally, J., Linke, R. A., Heiles, C., & Hurwitz, M. 1992, ApJS, 79, 77
- Stecker, F. W. 1996, in Unveiling the Cosmic Infrared Background, ed. E. Dwek (Woodbury, NY: AIP), 181
- Stecker, F. W., & de Jager, O. C. 1997, ApJ, 476, 712
- Wainscoat, R. J., Cohen, M., Volk, K., Walker, H. J., & Schwartz, D. E. 1992, ApJS, 83, 111
- Wheelock, S.L. et al. 1994, IRAS Sky Survey Atlas Explanatory Supplement, JPL Publication 94-11 (Pasadena:JPL)